

1 **Comparison of regolith physical and chemical characteristics with**  
2 **geophysical data along a climate and ecological gradient, Chilean Coastal**  
3 **Cordillera (26° to 38° S)**

4

5 Mirjam Schaller<sup>1\*</sup>

6 Igor Dal Bo<sup>2\*</sup>

7 Todd A. Ehlers<sup>1</sup>

8 Anja Klotzsche<sup>2</sup>

9 Reinhard Drews<sup>1</sup>

10 Juan Pablo Fuentes Espoz<sup>3</sup>

11 Jan van der Kruk<sup>2</sup>

12

13 <sup>1</sup> Department of Geosciences, University of Tübingen, Schnarrenbergstrasse 94-  
14 96, 72076 Tübingen, Germany

15 <sup>2</sup> Agrosphere (IBG-3), Institute of Bio- and Geosciences, Forschungszentrum  
16 Jülich, 52428, Jülich, Germany

17 <sup>3</sup> University of Chile, Department of Silviculture and Nature Conservation, Av.  
18 Santa Rosa 11315, La Pintana, Santiago RM, Chile

19 \* Authors contributed equally.

20

21 Corresponding author: E-mail: Mirjam Schaller (mirjam.schaller@uni-  
22 tuebingen.de)

23

24

25 **Abstract**

26 We combine geophysical observations from Ground Penetrating Radar (GPR)  
27 with regolith physical, and chemical properties from pedons excavated in four study  
28 areas spanning 1,300 km of the climate and ecological gradient in the Chilean  
29 Coastal Cordillera. Our aims are to: (1) relate GPR observations to depth varying  
30 regolith physical and weathering-related chemical properties in adjacent pedons,  
31 and (2) evaluate the lateral extent to which these properties can be extrapolated  
32 along a hillslope using GPR observations. Physical observations considered include  
33 regolith bulk density and grain size distribution, whereas chemical observations are  
34 based on major and trace element analysis. Results indicate that visually-  
35 determined pedolith thickness and the transition from the B to C horizons generally  
36 correlate with maximums in the 500 and 1000 MHz GPR envelope profiles. To a  
37 lesser degree, these maximums in the GPR envelope profiles agree with maximums  
38 in weathering related indices such as the Chemical Index of Alteration (CIA) and the  
39 chemical index of mass transfer ( $\tau$ ) for Na. Finally, we find that up-scaling from the  
40 pedon to hillslope scale is possible with geophysical methods for certain pedon  
41 properties. Taken together, these findings suggest that the GPR profiles down  
42 hillslopes can be used to infer lateral thickness variations in pedolith horizons in  
43 different ecologic and climate settings, and to some degree the physical and  
44 chemical variations with depth.

45

46 Keywords: regolith, pedolith, hillslope, climate, vegetation, geophysics,

47

48 **1 Introduction**

49 Weathering of bedrock by biotic and abiotic processes produces regolith which  
50 provides resources for life. Most biota is found in the mobile pedolith, which overlies  
51 the immobile saprolith. The pedolith is replenished with nutrients from the saprolith  
52 through chemical weathering and erosion that drives nutrient uplift towards the  
53 surface (e.g., Porder et al., 2007). The thickness and production of pedolith is  
54 influenced by aspect, topography, composition (mineral content), biota, climate,  
55 tectonically driven rock uplift, and time (e.g., Hilgard, 1914; Jenny, 1994). However,  
56 subsurface variations in pedolith thickness at the scale of hillslopes are difficult to  
57 quantify because of lack of exposure. Thus, subsurface imaging by geophysical  
58 techniques, when calibrated to regolith excavations (pedons), offers a potential  
59 means to characterize spatial variability in pedolith thickness and regolith properties  
60 (e.g., Mellett, 1995; Doolittle and Collins, 1995; Miller et al., 2002). Here, we  
61 evaluate the utility of applying Ground Penetrating Radar (GPR) to map variations  
62 in physical and chemical regolith properties caused by diverse climate and  
63 ecological settings.

64 Previous work has attributed spatial variations in pedolith thickness to hillslope  
65 curvature (Heimsath et al., 1997; Heimsath et al., 1999), which determines the  
66 downslope rate of mass transport assuming a diffusion-based geomorphic transport  
67 law (e.g., Roering et al., 2001). However, this single point information is spatially  
68 restricted and pedon excavations are time-intensive. To further understand spatial  
69 variations in pedolith and saprolith thickness, other approaches such as modeling  
70 (e.g., Scarpone et al., 2016) and geophysical imaging (e.g., see summary in  
71 Parsekian et al., 2015) have been applied. For example, pedolith thickness  
72 variations were extrapolated from Digital Elevation Models (DEMs) in combination  
73 with several different observations at single locations (e.g., Scarpone et al., 2016).  
74 Different geophysical techniques have provided a non- or minimally invasive  
75 approach to view pedolith variations down to the saprolith and bedrock interface  
76 (e.g., Parsekian et al., 2015). Whereas high frequency GPR has proven suitable for  
77 investigating pedolith layering and thickness (e.g., Doolittle et al., 2007; Gerber et

78 al., 2010; Roering et al., 2010; Dal Bo et al., 2019), other methods such as seismics  
79 (e.g., Holbrook et al., 2014), Electrical Resistivity Tomography (ERT, e.g., Braun et  
80 al., 2009), and low frequency GPR (e.g., Aranha et al., 2002) are better suited to  
81 image saprolite and bedrock interfaces (e.g., Parsekian et al., 2015). GPR methods  
82 were also previously used to indirectly measure water flow (e.g., Zhang et al., 2014;  
83 Guo et al., 2020) as well as root density (e.g., Hruska et al., 1999; Guo et al., 2013).  
84 Interpreting the interplay of GPR signals with physical and chemical regolith  
85 properties is challenging (e.g., Saarenketo, 199; Sucre et al., 2011; Tosti et al.,  
86 2013; Sarkar et al., 2019).

87 The Chilean Coastal Cordillera (Fig. 1) contains an extreme climate and  
88 vegetation gradient and is a natural laboratory to study the influence of climate and  
89 vegetation on the surface of the Earth in a setting with similar tectonic history and  
90 lithology. The region is home to four study areas of the German-Chilean EarthShape  
91 priority program ([www.earthshape.net](http://www.earthshape.net)), where investigations of biotic interactions  
92 with regolith were conducted (e.g., Bernhard et al., 2018; Oeser et al., 2018). The  
93 study areas were selected to show a range from arid climate in the northernmost  
94 location ( $\sim 26.1^\circ$  S), to temperate rain forest conditions in the southernmost location  
95 ( $\sim 37.8^\circ$  S). These four study areas were investigated to qualitatively and  
96 quantitatively describe the differences between the four settings. Our previous work  
97 in these areas has identified from field observations and GPR based methods an  
98 increase in pedolith thickness from north to south and major and trace element  
99 compositional variations within pedons (e.g., Bernhard et al., 2018; Oeser et al.,  
100 2018; Dal Bo et al., 2019). However, in our previous GPR work (Dal Bo et al., 2019)  
101 we were not able to present a detailed comparison of physical, chemical, and  
102 regolith observations which has yet to be reported for these areas.

103 In this paper we build upon the previous work of Dal Bo et al. (2019) and compare  
104 the pedon measured physical and chemical observations (from Bernhard et al.  
105 (2018) and Oeser et al. (2018)) to a large newly acquired GPR data set from the  
106 same area to gain insight into regolith variations along a climate and ecological  
107 gradient. Our approach is to relate GPR observations adjacent to pedons to depth

108 varying regolith properties caused by weathering as well as to evaluate if these  
109 properties can be extrapolated along a hillslope using GPR transects. In doing this,  
110 we test the hypothesis that if weathering processes produce depth varying physical  
111 and chemical changes in regolith observed in pedons, then (a) GPR based  
112 observations of these locations should produce observable changes in the GPR  
113 envelope and reflectors correlative to weathering horizons, and (b) GPR can be  
114 used to up-scale geochemical observations from pedons to the hillslope scale. In  
115 general, we find that our new GPR measurements can be correlated to changes in  
116 pedolith physical properties if these changes are of sufficient magnitude and laterally  
117 coherent. If such a correlation is observed, we discuss the links between the  
118 physical and chemical properties. The comparison of physical and chemical  
119 properties with field observations and GPR data helps to better understand the  
120 regolith at point locations (e.g., pedolith thickness) and in some cases allows for up-  
121 scaling point observations to the hillslope scale along a GPR measurement profile.  
122

## 123 **2 Study areas**

124 From north to south (Figs 1 and 2), the four selected study areas in the climatic  
125 and vegetation gradient observed in the Chilean Coastal Cordillera are: a) Pan de  
126 Azúcar (~26.1° S); b) Santa Gracia (~29.8° S); c) La Campana (~33.0° S); and d)  
127 Nahuelbuta (~37.8° S). The study areas were investigated for regolith physical and  
128 chemical properties by Bernhard et al. (2018) and Oeser et al. (2018) as well as  
129 studied with GPR by Dal Bo et al. (2019) (see Tables 1 and 2).

130

### 131 2.1 General climate, vegetation, and geologic setting

132 The Chilean Coastal Cordillera with its climate and vegetation gradient is a  
133 natural laboratory to study the influence of climate and vegetation on denudation  
134 (Fig. 1). From north to south (~26° to 38° S), present climate ranges from arid to  
135 humid-temperate. The mean annual precipitation increases from nearly zero to  
136 ~1500 mm yr<sup>-1</sup>, and mean annual temperature decreases from ~20° C to ~5° C.

137 Vegetation cover increases from nearly zero to ~100%. The flora consists of small  
138 shrubs, geophytes and annual plants (Armesto et al., 1993) in the north and  
139 changes to lower-stature deciduous trees and shrubs intermix with tall evergreen  
140 mixed forest in the south.

141 Climate and vegetation in the primary study areas changed over time from the  
142 Last Glacial Maximum (LGM) to present. Mean annual precipitation during the LGM  
143 was higher than at present in all four study areas (Mutz et al., 2018). Mean annual  
144 temperature during the LGM was lower than at present except in the southernmost  
145 study area where mean annual temperature stayed the same (Mutz et al., 2018).  
146 Hence, the climate gradient observed today is comparable to the gradient during the  
147 LGM. Even though the climate was wetter and cooler during the LGM, no glaciers  
148 covered any of the study areas (Rabassa and Clapperton, 1990). Because of these  
149 climatic changes over time, vegetation zones during the LGM were shifted  
150 northward by ~5° and vegetation cover was slightly (~5-10%) lower compared to  
151 present (Werner et al., 2018). This shift of vegetation zones to the north and the  
152 decrease in vegetation cover also likely influenced the fauna present, but to an  
153 unknown degree.

154 To compare the effect of climate and vegetation on pedolith thickness and GPR  
155 observations, differences in lithologies need to be minimal. However, these  
156 conditions are not always fulfilled and need to be taken in to account. Whereas  
157 bedrocks in Pan de Azúcar, La Campana, and Nahuelbuta are granites to  
158 granodiorites, the bedrocks in Santa Gracia range from Granodiorites to Gabbros  
159 (Oeser et al., 2018). Hence, the parent material in Santa Gracia is lower in SiO<sub>2</sub>-  
160 content (50-65%) in comparison to the other three study areas (SiO<sub>2</sub>-content >65%).  
161 Chemical weathering and physical erosion, which in turn influence pedolith  
162 formation and thickness, may be affected by this difference.

163

## 164 2.2 Regolith Characteristics

165 In each study area, regolith transects (Figs 2 and 3; Table 1) from a catena  
166 consisting of three pedons on the S-facing slope (top-slope, mid-slope, and toe-

167 slope) and one pedon on the N-facing slope (mid-slope) were described, sampled,  
168 and analyzed (see Bernhard et al., 2018; Oeser et al., 2018; Schaller et al., 2018;  
169 Dal Bo et al., 2019). Only one pedon was investigated in the N-facing slopes due to  
170 time and financial restrictions. In addition, transect lengths in some settings are  
171 limited due to the availability of weathered hillslopes in the same lithologies (e.g.,  
172 Pan de Azúcar; Fig. 3A) as well as restriction of access due to intense vegetation  
173 (e.g., Nahuelbuta; Fig. 3D).

174 These previous studies from pedons in each area identify O, A, B, and C horizons  
175 that overlie weathered bedrock (for complete characterization and interpretation of  
176 the pedons see Fig. 2 in Bernhard et al. (2018) and Figs 3 to 6 in Oeser et al. (2018)).  
177 In this study, we refer to depth profiles as regolith profiles that are composed of a  
178 mobile pedolith that includes the A and B horizons, and an immobile saprolith  
179 including the C horizon.

180 In Pan de Azúcar, the regolith, a regosol (IUSS Working Group WRB, 2015),  
181 consists of A and B horizons with a combined thickness of 20 to 25 cm and an  
182 underlying saprolith (the C horizon), which is coarse-grained and jointed (Oeser et  
183 al., 2018). The total organic carbon content of the A and B horizons is <0.1%  
184 (Bernhard et al., 2018). Angular fragments in the pedolith increase in size (> 1 mm)  
185 with depth. The average bulk density of the A and B horizons is 1.3 g cm<sup>-3</sup>. In Santa  
186 Gracia, the 30 to 55 cm thick pedolith overlying the saprolith is a cambisol (IUSS  
187 Working Group WRB, 2015). Total organic carbon content of the A and B horizons  
188 is 0.4%. Whereas the A horizon consists of a silt- to fine sand-sized matrix  
189 supporting up to 2 mm sized fragments, the underlying B horizon shows a  
190 transitional increase of fragments to a coarse fragment-supported fine-grained  
191 matrix. The weathered granodiorite of the saprolith consists of up to 1 cm-sized  
192 fragments which are surrounded by fine-grained material and fine roots (Oeser et  
193 al., 2018). The average bulk density of the pedolith is 1.5 g cm<sup>-3</sup>. The regolith in La  
194 Campana is a cambisol (IUSS Working Group WRB, 2015). The A and B horizons  
195 are 35 to 60 cm thick and have a total organic carbon content of 1.9% (Bernhard et  
196 al., 2018). The fine sand- to silt-sized A horizon contains fragments of up to 3 mm.

197 The matrix in the underlying B horizon is coarsening downwards and the number of  
198 fragments increases such that the horizon shifts from matrix- to clast-supported. In  
199 the saprolith, which shows a granodioritic fabric, fine roots are common and  
200 fractures are abundant (Oeser et al., 2018). The average bulk density is  $1.3 \text{ g cm}^{-3}$ .  
201 The regolith in Nahuelbuta, an umbrisol (IUSS Working Group WRB, 2015), consists  
202 of a 60 to 90 cm thick pedolith and a readily disaggregating saprolith. Total organic  
203 carbon content in these pedoliths is 6.1% (Bernhard et al., 2018). The A horizon is  
204 composed of silt-sized particles forming nodular aggregates. In the upper part there  
205 are up to 1 mm large quartz grains embedded whereas the lower part contains large  
206 fragments. The fine sand-sized matrix of the transitional B horizon hosts subangular  
207 fragments. The amount and size of these fragments increases with depth. The  
208 average bulk density of the pedolith is  $0.8 \text{ g cm}^{-3}$ .

209

### 210 **3 Data compilation and methods**

211 New data from 25 GPR profiles in the four study areas were collected at  
212 frequencies of 500 and 1000 MHz. These data are compared to physical and  
213 chemical properties from point locations (pedons) from previous studies (Bernhard  
214 et al., 2018; Oeser et al., 2018). Unfortunately, no regolith water content was  
215 measured in samples from the pedons excavated in 2016. The new GPR profiles  
216 (collected in 2017) complement previous GPR data collected 2016 at the same  
217 frequencies, in the same catchments (Dal Bo et al., 2019). The difference between  
218 this study and that of Dal Bo et al. (2019) lies in the new, more extensive, GPR data  
219 coverage, the analysis of regolith water content in augers in the study areas, and its  
220 comparison to physical and chemical subsurface variations.

221 Using physical and chemical properties collected in pedons to understand the  
222 corresponding radar signatures is a difficult task requiring multiple steps. First, it  
223 would require identifying relationships between the measured pedon properties and  
224 corresponding permittivity changes in the radar signal. Second, it would require a  
225 radar forward model that successfully predicts the convolution of the emitted radar



226 pulse with the subsurface reflectivity. This includes handling constructive and  
227 destructive interference caused by closely-spaced vertical permittivity changes. For  
228 applications to regolith this is currently not possible because the permittivity  
229 relationships are unclear. We therefore take a step back from the more  
230 sophisticated methods, and use simpler statistical metrics to isolate regolith  
231 properties (i.e. Pearson correlation) or combinations thereof (i.e. Principal  
232 Component Analysis) that may explain parts of the radar signatures.

233

### 234 3.1 Data compilation

235 In this study, GPR data are compared to previously published pedolith and  
236 saprolith physical and chemical properties (Table 2) such as: 1) bulk density, grain  
237 size distribution, acid and base properties - pH, and cation exchange capacity - CEC  
238 (Bernhard et al., 2018); and 2) Loss On Ignition - LOI, Chemical index of Alteration  
239 - CIA, mass transfer coefficient -  $\tau$ , and volumetric strain -  $\epsilon_{\text{strain}}$  (Oeser et al., 2018).  
240 The grain size distributions provide a measure of the weight percent of different  
241 grain sizes smaller than 2 mm in the regolith, and the bulk density provides a  
242 measure of how dense the pedolith and saprolith material is packed. The  
243 geochemical data used provide major and trace element analysis, pH, and CEC.  
244 Major and trace element analyses allow the investigation of the LOI, Tau  $\tau$ , and  
245 volumetric strain  $\epsilon_{\text{strain}}$ . The degree of weathering can be quantified by CIA which is  
246 sensitive to the removal of alkalis such as calcium, sodium, and potassium from  
247 feldspars (Nesbitt and Young, 1982).  $\tau_{\text{strain}}$  reflects chemical gains and losses  
248 during weathering based on the elemental concentrations of mobile and immobile  
249 elements in weathered and unweathered material (e.g., Brimhall et al., 1985;  
250 Chadwick et al., 1990),  $\epsilon_{\text{strain}}$  in a regolith is based on the density  $\rho$  ( $\text{g cm}^{-3}$ ) and  
251 immobile element concentrations of the weathered regolith in comparison to the  
252 unweathered bedrock indicating volumetric gain or loss (Brimhall and Dietrich,  
253 1987).

254 GPR signals are sensitive to regolith water content variations with depth (e.g.,  
255 Steelman et al., 2012; Ardekani et al., 2014). In addition to our compilation of  
256 previously published chemical and physical properties, we present here newly  
257 collected regolith water content data from regolith augers in Santa Gracia, La  
258 Campana, and Nahuelbuta (supplement Tables S3A to C). Although this data  
259 provides insight into regolith water content variations with depth, regularly spaced  
260 sampling with depth was not possible in the field. As a result, the regolith water  
261 content data are sparse, and not directly overlying the GPR profile locations. Given  
262 the sparseness of this data, we were not able to include it in our correlations or  
263 correlation and PCA analysis (described below), but we do discuss trends present  
264 in the regolith water content (gravimetric basis) with depth and potential implications  
265 for the rest of our analysis. Furthermore, we note that the GPR data were not  
266 collected with an approach that allowed for the inversion for regolith water content  
267 (e.g., Steelman et al., 2012).

268

### 269 3.2 Ground Penetrating Radar (GPR)

270 Ground Penetrating Radar (GPR), a geophysical technique based on the  
271 emission of pulsed electromagnetic waves into the subsurface, are applied in this  
272 study for frequencies of 500 and 1000 MHz (for more details see Dal Bo et al., 2019).  
273 Fourteen new transects going from hillslope toe (near valley) to top (ridge crest) are  
274 collected crossing the pedons where physical and chemical properties were  
275 collected (Figs. 2 and 3). Of these 14 transects, two were collected in the Pan de  
276 Azúcar study area (for 500 and 1000 MHz), six in Santa Gracia (for 500 and 1000  
277 MHz), three in La Campana (for 500 and 1000 MHz), and three in Nahuelbuta (only  
278 for 500 MHz). Wide-angle-reflection-refraction (WARR) are used to retrieve velocity  
279 and physical properties at the point scale. For each pedon, a WARR is measured in  
280 a relatively flat location (red stars, Fig. 2).

281 GPR data were processed and analyzed using MATLAB as described in Dal Bo  
282 et al. (2019). In addition, signal envelopes were calculated using a Hilbert transform  
283 (Green, 2004; Liu and Marfurt, 2007). At each pedon location, a certain number of

284 traces depending on the measurement step size (i.e. between 10 and 50) were  
285 sampled for 0.5 m uphill and 0.5 m downhill the pedon and laterally averaged for  
286 comparison to the pedon physical and chemical properties. The averaging assumes  
287 that both chemical and GPR signatures do not change with depth across that  
288 interval, an assumption that may not hold everywhere. As the GPR envelope is  
289 directly related to the electric impedance (Telford et al., 1990; Jol, 2009), the  
290 envelope onset and energy intervals could be compared to variations in physical,  
291 and potentially chemical, regolith properties.

292

### 293 3.3 Statistical Correlation and Principal Component Analysis

294 Comparison between the physical and chemical pedon information (Bernhard et  
295 al., 2018; Oeser et al., 2018) and GPR data was conducted. Where available, we  
296 used the bulk density, clay content, LOI, CIA, Tau ( $\tau$ ), volumetric strain ( $\epsilon_{\text{strain}}$ ), pH,  
297 and CEC for comparison to the GPR 500 and 1000 MHz antennae envelope data.  
298 The GPR envelopes were resampled and averaged, such that the depth intervals  
299 were the same as for the derivatives of the regolith data (see Table S2). Furthermore,  
300 because the envelope of GPR data is sensitive to changes along the vertical  
301 direction, we also calculated the vertical gradient of the ground truth information at  
302 each sampled depth using a centered difference approximation. Following this, the  
303 R package function `corrplot` (Wei, 2012) was used to calculate the Pearson's  
304 correlation coefficient to identify correlations between the variables (Sedgwick,  
305 2012). We further conducted a multivariate analysis of the data based on principal  
306 component analysis (PCA; Wold et al., 1987). This was done using the `factoextra` R  
307 package (Kassambara, 2017). Correlation coefficients and PCA are done for each  
308 study area along the entire climate gradient.

309

## 310 **4 Results**

311 Physical and chemical properties of pedons are shown with the 500 and 1000  
312 MHz GPR profiles and their envelopes with depth as well as investigated

313 correlations and PCA results for the four study areas (Figs 4 to 11; Figs S1 to S12;  
314 Table 3; Tables S1A to D, S2A to D, S3A to C, and S4A to E). For brevity,  
315 comparisons between pedon observations and GPR data are presented only for the  
316 S-facing mid-slope positions in the main text (Figs 4, 6, 8, and 10) and the remaining  
317 locations are provided in the supplementary material. Note that the envelopes are  
318 averaged over the common offset profile data, collected over a lateral distance of 1  
319 m in total, and are therefore not point information. Given that the pedolith thickness  
320 increases towards the southern study areas, the 1000 MHz GPR antenna is  
321 interpreted for the northern two study areas Pan de Azúcar and Santa Gracia,  
322 whereas in La Campana and Nahuelbuta the 500 MHz GPR signal was used  
323 because it has a deeper penetration depth. However, we show results below for  
324 both frequency antennas to demonstrate the difference in penetration depth and  
325 resolution between the two antennae. Details for each study area (from north to  
326 south) follow.

327

#### 328 4.1 Pan de Azúcar (northern most and driest study area)

329 In Pan de Azúcar (Figs 1 and 2A), a gradual transition from the B to the C horizon  
330 was visually observed in the pedons at 20 to 40 cm (shaded gray areas after  
331 Bernhard et al. (2018); Fig. 4; Figs S1 to S3), whereas the mobile and immobile  
332 boundary is considered to be at 20 to 25 cm (black lines after Oeser et al., (2018);  
333 Fig. 4; Figs S1 to S3). No water content measurements for this area were available  
334 due to poor recovery of auger samples from the impenetrable substrate. The  
335 available physical properties for this location do not indicate a strong change in  
336 material properties with depth. LOI and CIA indicate a minor change in properties at  
337 ~20 cm depth. A maximum in the energy envelope in the 1000 MHz frequency is  
338 present at about 20 to 30 cm, and could be related to the transition of material  
339 properties between the B and C horizons and the location of mobile and immobile  
340 boundary observed in the field.

341 Due to the sparse depth information for bulk density and clay content, the  
342 statistical analyses for this location were not very insightful. Whereas clay content

343 shows a medium correlation (0.54) with the 1000 MHz GPR envelope, no strong  
344 correlation between LOI, CIA, Tau  $\tau$ , and the 1000 MHz GPR envelope could be  
345 found (Table 3). In the PCA, three principal components (PC) explain over 80% of  
346 the variance (Table S4A). PC1 has the biggest contribution from CIA, clay content,  
347 and the 500 MHz envelope whereas PC2 has the biggest contribution from LOI, the  
348 1000MHz envelope, and  $\tau$  of Na and Zr (Fig. 5).

349

#### 350 4.2 Santa Gracia

351 In Santa Gracia (Figs 1 and 2B), a gradual transition from the B to the C horizon  
352 was observed in the field between 20 to 60 cm depth (shaded gray region Fig. 6;  
353 Figs S4 to S6). The boundaries between the pedolith and saprolith were observed  
354 between 30 to 55 cm depth. Water content near pedon locations ranges between  
355 7.6% to 1.8% and is highly variable with sample locations and with no clear spatial  
356 or depth dependent trend (Table S3A). Bulk density and volumetric strain show  
357 slight changes around 15 and 30 cm depth. Whereas LOI and CIA do not show any  
358 changes with depth,  $\tau$  shows changes between 30 and 50 cm depth. The 500 and  
359 1000 MHz GPR profiles and envelopes show increased irregular and strong  
360 reflections at ~25 cm (1000 MHz) and 45 cm (500 MHz) depth, and also maximums  
361 in the envelope at ~25 cm (1000 MHz) and 45 cm (500 MHz) depths. These  
362 variations in the reflections and maximums in the envelopes coincide with either the  
363 top or central position of the transition from the B to the C horizon.

364 A weak to moderate correlation (~0.30) between clay content as well as CIA and  
365 the 1000 MHz GPR envelope is present (Table 3). Results from a PCA analysis of  
366 the Santa Gracia data indicate that 3 components explain over 80% of the observed  
367 variance (Table S4B). PC1 explains over 35% of the variance, and includes bulk  
368 density, CIA, and the 500 and 1000 MHz envelopes (Fig. 7). PC2, explaining 31%  
369 of the variance, includes clay content, LOI, and  $\tau$  of Na and Zr.

370

#### 371 4.3 La Campana

372 Field observations from the La Campana area (Figs 1 and 2C) document a layer  
373 of cobbles (5 to 10 cm diameter) between the A and B horizon at a depth of ~30 cm  
374 (Bernhard et al., 2018). The transition between the B to C horizons does not contain  
375 rock fragments. The transition from the B to C horizon (shaded gray area, Fig. 8)  
376 and the mobile and immobile boundary (black line, Fig. 8) are observed at 34 to 110  
377 cm and 35 to 60 cm, respectively (see also Figs S7 to S9). The pedolith extends  
378 deeper in La Campana than in Pan de Azúcar or Santa Gracia and physical  
379 properties were available for greater depths. Bulk density and grain size change  
380 gradually with depth and no pedolith thickness could be determined. Also, LOI, CIA,  
381 and  $\tau$  do not show an abrupt change in regolith properties. Water content near  
382 pedons ranges between 3.1% to 1.5% and shows only a slight (~0.5%) decrease  
383 between depths of ~30 to 90 cm (Table S3A). Reflection hyperbolas and irregular  
384 reflection horizons appear in the 500 and 1000 MHz GPR data at about 40 to 60 cm  
385 depth above the B to C horizon transition. The second peaks of the 500 and 1000  
386 MHz GPR envelopes coincide with the B to C horizon transition.

387 In contrast to the previous study areas, the 500 MHz GPR envelope correlates  
388 moderately with CIA (0.56), pH (-0.57), and CEC (-0.39, Table 3). Three  
389 components from the PCA analysis explain about 80% of the total variance (Table  
390 S4C). PC1 (~35% of the total variance) includes LOI, Tau  $\tau$ , and CEC, whereas PC2  
391 (31%) contains CIA, volumetric strain  $\varepsilon_{\text{strain}}$ , and the envelopes (Fig. 9). PC3 is  
392 dominated by pH as well as  $\tau$  of Zr. In general, whereas the first energy interval  
393 (1000 MHz) could be attributed to the stone layer between the A and B horizon, the  
394 second energy interval occurs close to (<10 cm) with the mobile and immobile  
395 boundary (Fig. 8).

396

#### 397 4.4 Nahuelbuta (southernmost and wettest study area)

398 In Nahuelbuta, the B horizon contains pebbles and cobbles at around 60 to 80  
399 cm depth (Bernhard et al., 2018). The B to C horizon transition appears at 50 to 100  
400 cm depth (shaded gray region, Fig. 10; see also Figs S10 to S12). The mobile and

401 immobile boundary was identified at 60 to 90 cm depth (Oeser et al., 2018). Density  
402 measurements in the pedon indicate a transition in bulk density between about 30  
403 to 60 cm depth where the grain size distribution also changes. The LOI and  $\tau$   
404 generally show large changes with depth, in contrast to the CIA and volumetric strain  
405 which are more homogenous with depth. In general water content near pedons and  
406 in near-surface (10 to 30 cm depth) samples is between 23 and 39% and decreases  
407 ~3% to ~10% over regolith depths of 30 to 90 cm (Table S3A). In addition, water  
408 content increases from top- to toe-position in the S-facing slope and is lower in the  
409 N-facing mid-slope position than in the S-facing position. The 500 MHz GPR profile  
410 indicate the existence of point targets/objects appearing as reflection hyperbola or  
411 undulating features at depths greater than 60 cm. This depth is approximately the  
412 same depth at which the mobile and immobile boundary was identified, as well as  
413 changes in the physical properties (e.g. bulk density, percent sand) and chemical  
414 properties (LOI, Tau  $\tau$ ). The hyperbolas do not add up coherently during the lateral  
415 averaging and therefore do not produce a significant energy interval in the average  
416 envelope. The envelope is dominated by the energy intervals given by two  
417 reflections at about 30 to 50 cm depth. The lower set of these energy intervals could  
418 be linked with the upper physical pedolith boundary.

419 Results from the correlation analysis indicate that the 500 MHz GPR envelope  
420 is strongly positively correlated with bulk density (0.74), strongly inversely correlated  
421 with LOI (-0.60), and moderately inversely or positively correlated with clay content  
422 (-0.37), pH (0.46), and CEC (-0.53) (Table 3). Results from the PCA analysis show  
423 that two PC components explain ~75% of the variance. PC1 (~57 %) includes bulk  
424 density, clay content, LOI, and CEC, and PC2 (~18 %) contains  $\tau$  of Zr and pH (Fig.  
425 11; Table S4D). In general, as the 500 MHz GPR envelope signal correlates well  
426 with bulk density and clay content, the envelope signal reflects changes in regolith  
427 properties.

428

429 **5 Discussion**

430 Here we evaluate the physical, chemical, and geophysical observations from the  
431 pedons. Using this information, we attempt to up-scale information from the pedons  
432 to the hillslopes scale along the GPR transects.

433

434 **5.1 Synthesis of GPR data with physical and chemical properties from point**  
435 **locations**

436 GPR data image subsurface changes that could be caused by variations in  
437 physical (e.g., bulk density, grain size variation, water content) and chemical  
438 properties (e.g., pH, CEC, CIA). The interplay between these different properties  
439 can have a complicated influence on the GPR signal and therefore can be difficult  
440 to disentangle. Disentangling any relationship between GPR data and physical and  
441 chemical properties is further complicated because not all properties influencing  
442 GPR data are measured in the pedons (e.g., water content; Jol, 2009). In addition,  
443 the determination of the boundary between the pedolith and saprolith in the field  
444 causes its own problems because observed changes are not discrete but  
445 transitional over a depth interval of 5 to 10 cm. In the following, we start by  
446 discussing if GPR data can be used to image pedolith thickness as well as physical  
447 and chemical properties at the pedon locations where *in-situ* observations were  
448 made in each study area.

449 In Pan de Azúcar (Figs 4 and 5; Figs S1 to S3), the locations where GPR data  
450 can be compared to pedons show low variability in the observed pedolith thickness  
451 (~20 to 30 cm) at each pedon location. Whereas the 500 MHz signal shows the  
452 interface with the saprolith, the maximum in the 1000 MHz energy interval signal  
453 agrees with the pedolith thicknesses observed in the field (Fig. 4 and Figs S1 to S3).  
454 However, the boundary between the pedolith and saprolith is probably too shallow  
455 to be detected with the 1000 MHz antenna. An even higher frequency would be  
456 required to detect the pedolith and saprolith boundary. Hence the Pearson  
457 correlations and PCA results from Pan de Azúcar are restricted not only because of  
458 GPR analysis but also due to restricted physical properties. The physical and



459 chemical properties correlate only weakly to moderately with the 1000 MHz  
460 envelopes (Table 3). The PCA results indicate that bulk density is not likely  
461 correlated with either the 1000 MHz signal or LOI. In Pan de Azúcar, LOI does not  
462 represent organic matter because regoliths of arid zones generally have low or no  
463 organic matter content. The volatile loss measured in the LOI is more likely  
464 associated with the combustion of carbonates. In general, shallow pedoliths in the  
465 arid zone do not show much variability in pedolith thickness nor do they provide  
466 insight into the influence of physical or chemical properties on GPR signals.

467 In Santa Gracia (Figs 6 and 7; Figs S4 to S6), the field-observed pedolith  
468 thicknesses of the different pedons are more variable than in Pan de Azúcar.  
469 Although the 500 MHz and 1000 MHz GPR envelopes indicate changes at depth,  
470 the physical and chemical properties observed with depth show only a few distinct  
471 changes implying that the pedolith thickness cannot easily be determined using only  
472 physical or chemical properties. The PCA indicates that most of the variance in PC1  
473 is explained by the envelope signals, bulk density, and CIA whereas PC2 is  
474 dominated by clay content and Tau  $\tau$  of Na and Zr. The clay content does not seem  
475 to be a dominant factor for the envelope signal, but rather represents a complex  
476 interaction between physical and chemical property changes that cannot be  
477 disentangled with available data. It appears that the second energy interval in the  
478 1000 MHz envelope may agree with the observed pedolith thickness in Santa  
479 Gracia, and (in contrast to the Pan de Azúcar location) the first maximum in the 500  
480 MHz envelope does agree with the observed pedolith thickness. These  
481 observations again underscore, that for different locations with variable regolith  
482 type, vegetation, and physical and chemical properties local calibration between  
483 pedons and GPR data are required.

484 The determination of pedolith thickness from GPR data in La Campana is as  
485 difficult as in the previous settings (Figs 8 and 9; Figs S7 to S9). Field observations  
486 indicate relatively thick transition zones from the B to C horizons, and some physical  
487 properties vary only weakly with depth. As a result, the determination of pedolith  
488 thickness with physical and chemical properties is difficult, despite the moderate to

489 strong correlation of 500 MHz GPR envelopes with derivatives of physical and  
490 chemical properties. Whereas PC1 explains much of the variance in terms of bulk  
491 density, LOI, Tau  $\tau$  of Na and Zr, and volumetric strain  $\epsilon_{\text{strain}}$ , the PC2 consists out  
492 of the envelopes, CIA, pH, and CEC. Chemical properties seem to have a  
493 considerable influence on GPR signals in this setting. In La Campana, the first  
494 energy interval in the 500 MHz envelope is interpreted to reflect the presence of the  
495 stone layer whereas the second energy interval seems to match the observed  
496 pedolith thickness. Given these uncertainties in local conditions, a clear  
497 identification of pedolith thickness from GPR data is difficult, even with local  
498 calibration to a pedon.

499 Finally, in Nahuelbuta (Figs 10 and 11; Figs S10 to S12), the observed pedolith  
500 thickness in the field is the deepest of all the four study areas and reaches from 50  
501 to 100 cm. The pedolith thickness is easily identifiable based on physical properties  
502 (e.g., bulk density, grain size variation). The derivatives of the physical properties  
503 correlate moderately with the available 500 MHz envelope (Table 3). Furthermore,  
504 the chemical properties correlate weakly with the GPR envelope. The variance is  
505 strongly explained by PC1 containing physical properties (e.g., bulk density, clay  
506 content, LOI) and less by PC2 including chemical properties (e.g., pH, Tau  $\tau$  of Na  
507 and Zr). Even though changes in properties are more pronounced in Nahuelbuta  
508 than in the drier locations, a clear correlation between maximums in the 500 MHz  
509 energy envelope and pedolith thickness is not present. The second energy interval  
510 of the 500 MHz envelope best agrees with the observed pedolith thickness.  
511 However, due to local inhomogeneities caused by intense vegetation, every pedon  
512 and its attributed GPR envelope looks different.

513 In summary, the 500 and 1000 MHz envelopes at point locations have the  
514 potential to be used to determine pedolith thickness. But the clarity with which this  
515 can be done is variable and requires calibration to local pedons. Even with local  
516 calibration, the relationships are not always clear (e.g., Fig. 8). Physical and  
517 chemical properties with depth exert a complex influence on measured GPR signals.  
518 If a certain combination of physical and chemical properties is dominant in one

519 setting, another combination may influence the measured GPR signal in another.  
520 For example, whereas clay content correlations are moderately positive with GPR  
521 envelopes in the dry area of Pan de Azúcar, the relationship is weaker at more  
522 southerly latitudes and is moderately negatively correlated in Nahuelbuta. Other  
523 physical properties (e.g., bulk density, LOI) only correlate well with the envelopes in  
524 the southernmost study area of Nahuelbuta. The more pronounced correlation of  
525 bulk density and LOI with the envelope signal can be attributed to the abundance of  
526 organic matter in the regolith. The presence of organic matter influences not only  
527 bulk density and LOI but also CEC and pH (all organic matter related variables).  
528 Analysis of the PCA results in light of organic matter variations identifies the  
529 following variables as being best explained from north to south: (1) in Pan de  
530 Azúcar: the GPR envelope, clay content, and CIA are most closely related; (2) in  
531 Santa Gracia: the GPR envelope, bulk density, and CIA are most closely related;  
532 (3) in La Campana: the GPR envelope, bulk density, organic matter related variables  
533 are related; and (4) in Nahuelbuta: the organic matter related variables, bulk density,  
534 and GPR envelope are most closely related.

535 Thus, the influence of vegetation and the continuous addition of organic matter  
536 to regolith properties influencing GPR signals are strengthened from north to south.  
537 Therefore, which GPR frequency works best for the individual study area (due to  
538 different physical and chemical properties) needs to be investigated with information  
539 from point locations/pedons. For the arid Pan de Azúcar and semi-arid Santa Gracia  
540 we suggest using the 1000 MHz frequency (or higher), whereas for the  
541 Mediterranean climate setting of La Campana and temperate Nahuelbuta the 500  
542 MHz frequency proved better. Improvements in our approach to determine pedolith  
543 thickness from GPR data might be possible by applying multifrequency GPR  
544 techniques, which are freed from antenna effects by fusion of different frequency  
545 measurements (e.g., De Coster and Lambot, 2018). Nevertheless, the point  
546 information of pedolith thickness has the potential to be up-scaled to hillslopes in  
547 some settings using GPR transects after local calibration is conducted.

548

## 549 **5.2 Up-scaling to hillslopes**

550 Here we use insights gained from comparisons between GPR and point  
551 locations to extrapolate the pedolith thickness along the hillslope GPR profiles (Figs  
552 2 and 3). Our efforts here complement previous work by Dal Bo et al., (2019) by  
553 adding 25 new GPR profiles that cover a larger geographic region. The up-scaling  
554 is carried out using a combination of amplitude and envelope depth-converted  
555 profiles. To do this up-scaling, we calculated the envelope along each profile. Then,  
556 using the known pedolith depth data from all pedons in one study area, this interface  
557 was estimated along the profiles by searching for the corresponding signal in the  
558 envelope at every meter. Even though the information of three-point locations is at  
559 the lower limit, the combination of field observations with GPR transects allows  
560 estimation of the lateral variability of pedolith thickness over hillslopes. However, the  
561 complications which frequency of GPR antenna to use for analysis (Dal Bo et al.,  
562 2019) in addition to what envelope interval to select (section 5.1) requires careful  
563 up-scaling of the pedolith thickness to hillslopes.

564 In Pan de Azúcar (Fig. 12; Fig. S14) the observed B to C horizon transition at  
565 point locations is typically between ~14 to 50 cm. No clear pedolith thickness could  
566 be determined based on GPR profiles. Nevertheless, pedolith thicknesses identified  
567 from 1000 MHz GPR envelopes seem to be relatively homogeneous over the entire  
568 S-facing transect with an average value of  $25 \pm 3$  cm (Table 1). In contrast, the N-  
569 facing transect indicates a thinner pedolith uphill than downhill where it reaches a  
570 maximum depth of ~50 cm (Fig. S14). In Santa Gracia (Fig. 13; Figs S15 to 17), the  
571 pedolith thicknesses from point locations/pedons in the S-facing transect increases  
572 downslope and ranges between 20 to 60 cm (Table 1). The pedolith thickness based  
573 on the 1000 MHz GPR envelope at the top-slope position (SGPED20) decreases  
574 first downhill and then increases again, thereby demonstrating laterally variability  
575 down the hillslope. The pedolith thickness in the mid-slope position (SGPED40) is  
576 variable and reaches from 25 to 50 cm. At the toe-slope position (SGPED60) a  
577 mostly constant thickness of 30 cm is identified. In the N-facing transect almost no  
578 variability in pedolith thickness (~25 cm) is observed. Although the pedolith

579 thickness based on GPR envelopes cannot be used to decipher the exact pedolith  
580 thickness, the method still offers a close approximation of pedolith thicknesses  
581 determined by field observations and GPR profiles. In La Campana (Fig. 14; Figs  
582 S18 to 20) the pedolith thickness from the 500 MHz GPR envelope is 35 to 70 cm  
583 (Table 1). Whereas the top- and mid-slope positions in the S-facing hillslope  
584 (LCPED10 and LCPED20, respectively) show variable pedolith thickness between  
585 50 and 70 cm, the toe-slope position (LCPED30) contains pedolith thicknesses  
586 between 35 and 70 cm. Relatively constant pedolith thickness of 50 to 60 cm are  
587 identified for the N-facing mid-slope position (LCPED40). Field observations do not  
588 always agree with pedolith thicknesses based on GPR envelopes. In the La  
589 Campana location, pedolith thicknesses based on GPR envelopes need to be  
590 considered with caution, but contain valuable information such as the existence of  
591 pebble layers. However, GPR profiles show hyperbolas and continuous reflections,  
592 which can be interpreted along almost all the covered length. These interfaces can  
593 be reliably used to infer pedolith thicknesses, when a previous calibration with  
594 pedons has been done. In Nahuelbuta (Fig. 15; Figs S21 to 23), pedolith thickness  
595 in the S-facing top-slope position (NAPED10) increase downhill from 60 to 110 cm  
596 (Table 2). At the mid-slope position (NAPED20), the pedolith thickness is highly  
597 variable and ranges from 50 to 110 cm. Pedolith thickness at the toe-slope position  
598 (NAPED30) is 80 to 110 cm. In the N-facing mid-slope position the pedolith  
599 thickness ranges from 60 to 110 cm. Pedolith thicknesses based on GPR envelopes  
600 are generally thicker than pedolith thicknesses observed in the field and do also not  
601 agree well with thicknesses based on GPR profiles. The discrepancy between GPR  
602 measurements and field observations could result from the high water content in  
603 Nahuelbuta at the time of GPR acquisition. Alternatively, the discrepancy could also  
604 result from the heterogeneity of regolith observed in pedons at each location  
605 (Berhard et al., 2018). The application of GPR envelopes to determine pedolith  
606 thicknesses needs to be treated with care in this setting. On the contrary, GPR  
607 profiles display rather continuous reflections that might represent interfaces within

608 the pedolith, and could therefore be used to extrapolate point-scale ground-truth  
609 information over the profile scale.

610 In summary, the application of GPR envelopes to determine pedolith thicknesses  
611 provides more information than pedolith thicknesses determined from GPR  
612 transects alone where in some cases no clear reflections may be visible. Generally,  
613 the findings of this study agree with the findings of Bernhard et al. (2018) as well as  
614 Dal Bo et al., (2019). Pedolith thicknesses increase from north to south in latitude.  
615 Due to the increase in vegetation amount pedolith thicknesses are also less  
616 homogenous from increasing latitude (north to south). Due to the increasing  
617 heterogeneity in pedolith thickness, no clear trend in increasing pedolith thickness  
618 from top- to toe-slope is easily detectable. Only in Santa Gracia, the constantly thin  
619 pedoliths at the S-facing top-slope are in contrast to the thicker and more variable  
620 pedolith thickness in the mid-slope position. Bernhard et al., (2018) describe an  
621 increase of the A to BC horizon from top- to toe-slope in the S-facing hillslope. In  
622 addition, a clear difference between pedolith thickness from S- and N-facing slopes  
623 could not be detected for the more heavily vegetated study areas in the south.  
624 Again, only in Santa Gracia with little vegetation an expected difference in pedolith  
625 thickness between S- and N-facing slopes was detectable. The increase in  
626 vegetation under increasing precipitation rates causes not only more heterogenous  
627 pedolith depths, but also stabilization of hillslopes (e.g., Langbein and Schumm,  
628 1958; Schmid et al., 2018; Starke et al., 2020).

629

### 630 **5.3 Comparison to previous work and study caveats**

631 Geophysical studies focusing on the critical zone are a relatively new topic and  
632 have gained emphasis in the past decades (e.g., Parsekian et al., 2001). The results  
633 presented in this study complement a range of previous studies. Previous studies  
634 have used near surface geophysical methods to non-invasively measure subsurface  
635 properties and structures of the regolith and help to characterize critical zone related  
636 processes in the shallow subsurface (e.g., Scott and Pain, 2009). In this study, we  
637 focused in particular on deploying surface ground penetrating radar (GPR). The

638 electromagnetic properties of the subsurface affect the propagation (i.e. velocity),  
639 attenuation (i.e. the energy loss), and reflectivity of the electromagnetic waves (e.g.,  
640 Jol, 2009). The electromagnetic wave velocity and attenuation can be linked to the  
641 dielectric permittivity and electrical conductivity of the subsurface, respectively.  
642 Previous work provides examples of environments, where GPR is suitable for  
643 mapping subsurface properties. These include karst areas, where structures in the  
644 regolith have been identified up to the bedrock interface (e.g., Estrada-Medina et  
645 al., 2010; Fernandes Jr. et al., 2015; Carriere et al., 2013), volcanic environments  
646 (e.g., Gomez et al., 2012; Ettinger et al., 2014), and dry environments (e.g., Bristow  
647 et al., 2007; Harari, 1996) as generally these regimes are characterized by low clay  
648 and water content. The primary new contribution of this study with respect to existing  
649 regolith studies is the comparison of GPR data to a wide range of physical and  
650 chemical properties that are commonly interpreted in projects studying surface  
651 processes.

652 Previous work has highlighted the primary factors that GPR data can be sensitive  
653 to, and we briefly discuss these in the context of caveats associated with our work.  
654 Important factors that influence GPR data are the presence of water, solute content,  
655 and conductive materials such as clay (e.g., Scott and Pain, 2009; Huisman et al.,  
656 2003). In particular, clay as a highly conductive material has a significant impact on  
657 GPR signal as it affects the permittivity and the electrical conductivity at the same  
658 time (e.g., Daniels, 2004). With increasing amounts of clay in the subsurface, the  
659 signal penetrating is decreased due the increased attenuation of the waves.  
660 However, this behavior can be used to identify fine material in the subsurface, since  
661 in GPR profiles clay layers could be identified starting from spatial differences in  
662 signal penetration (e.g., Gómez-Ortiz et al., 2010; De Benedetto et al., 2010; Tosti  
663 et al., 2013). Furthermore, particle size beyond just clay content also plays a major  
664 role in GPR measurements, as the closer the particle size is to the wavelength of  
665 the emitted electromagnetic waves, the stronger are the reflections generated by  
666 these particles that can be seen in the detected signals (e.g., Jol, 2009). In this

667 study, we incorporated clay content into our PCA and correlation analysis to identify  
668 if, and by how much, it may influence GPR observations.

669 Previous studies have also documented how mineralogical variations with depth  
670 influence GPR signals. For example, the presence of minerals such as iron and  
671 aluminum oxides/hydroxides can play an important role in limiting the depth of  
672 penetration for GPR waves (e.g., Čeru et al., 2018) as iron-oxides have been linked  
673 with variations of relative permittivity, which might have in turn a considerable effect  
674 in the propagation of the GPR signals and effect the interpretation (e.g., Van Dam  
675 et al., 2003; Van Dam and Schlager, 2000; Havholm et al., 2003). Other studies  
676 showed that with increasing mafic mineral content in the subsurface, GPR signal  
677 attenuation is higher (e.g., Breiner et al., 2011). The presence of clay lenses in the  
678 regolith, alongside the layering, can influence the preferential flow path for regolith  
679 water, which can enhance reflectivity of the surfaces and therefore produce  
680 detectable reflections (e.g., Zhang et al., 2014). In this study, mineralogical  
681 variations with depth in the pedons were not available for comparison to our GPR  
682 data. However, we note that many of the processes described above may be  
683 responsible for the subsurface reflectors observed in Figures 12 to 15, and the fairly  
684 uniform granitoid composition of the different study areas means that mineralogical  
685 variations along any given hillslope profile are likely minimal and not a dominant  
686 source of signal in our GPR data.

687 The presence of volumetric water limits GPR signal penetration, with an  
688 increasing effect at higher frequencies (e.g., Utsi, 2017; Miller et al., 2002). GPR  
689 techniques have been used in the past two decades as a tool to detect water content  
690 variations in the subsurface as it has a strong effect on the dielectric permittivity  
691 (e.g., Klotzsche et al., 2018). In compact regoliths, where the volumetric water  
692 content is small, it has been shown that the bulk density has an important effect on  
693 the wave velocity, which is positively correlated (Wang et al., 2016). When solutes  
694 are present in the groundwater, the electrical conductivity of the medium increases,  
695 generating more signal loss, and therefore increasing wave attenuation (e.g.,  
696 Benedetto and Palewski, 2015). One shortcoming of our study is that no information



697 about subsurface water content within the pedon depth profiles was available for  
698 comparison to GPR observations as we did with the regolith physical and chemical  
699 properties. The depth varying chemical weathering indices we present (e.g., CIA,  
700 Tau, Fig. 4 to 10) would not be expected to correlate with present-day water content  
701 as these weathering indices developed over the timescale of regolith development  
702 (millennia and longer). Nevertheless, we find that out of the four study areas  
703 investigated, the present-day water content appears to influence the GPR signals  
704 and interpretations presented here only in the southernmost and wettest study area  
705 Nahuelbuta. As a result, the subsurface correlations between the GPR envelopes  
706 and physical or chemical properties at this location are likely influenced, to an  
707 unknown degree, by regolith water content. The exclusion of regolith water content  
708 in our analysis may very well be a reason why we are not able to explain the full  
709 radar signature. Although without the inclusion of this data, peaks in the radar  
710 envelopes were still interpretable when compared to available physical and  
711 chemical property variations with depth. Thus, although the inclusion of regolith  
712 water content would be preferred, the omission of it does not negate the observed  
713 signals we were able to interpret.

714 In locations, where the aforementioned regolith properties are not dominant, GPR  
715 can be used as a tool to identify structures and layering in both sediments (e.g.,  
716 Bristow and Jol, 2003) and regoliths, where interfaces ranging from the regolith-  
717 bedrock limit to the B horizon have been identified due to changes in the dielectric  
718 permittivity (e.g., Yoder et al., 2001; Lambot et al., 2006). In particular Zhang et al.  
719 (2018) showed the potential of mapping regolith layering in grasslands obtaining  
720 differences between GPR reflections and real regolith layer depth within 3 cm. In  
721 many situations, the interplay between different regolith properties make it difficult  
722 to understand the subsurface architecture without validation through regolith  
723 samples, as shown by Orlando et al. (2016) in the Rio Icacos watershed (Puerto  
724 Rico), where the stress regime, climate, and lithology are controlling the structures  
725 visible in GPR profiles. In comparing the previous studies to this one, we note that  
726 'in general' the results of this study were able to identify subsurface regolith structure

727 and explain them, in many cases, with available physical and chemical properties.  
728 However, the complexity in GPR signals observed necessitates having pedons for  
729 local calibration when comparing to regolith weathering indices.

730

## 731 **6 Conclusions**

732 Pedolith thickness and physical and chemical properties are investigated in four  
733 study areas along a climate and vegetation gradient. This gradient spans from arid  
734 and Mediterranean to temperate humid conditions. The visually observed transition  
735 from the mobile pedolith to immobile saprolith coincides with one or more changes  
736 in measured physical and chemical properties in each study area. These physical  
737 and chemical properties in turn, influence return signals generated by Ground  
738 Penetrating Radar (GPR) in the regolith, but no systematic trend is visible for which  
739 physical or chemical properties correlate with GPR based observations of pedolith  
740 thickness. Given this, the measurements and interpretation of GPR signals for  
741 systematically identifying subsurface changes in physical and chemical properties  
742 is not straightforward and differs for each study area. In general, the better  
743 developed the pedolith the better the correlation of GPR signals from point locations  
744 with physical and chemical regolith properties. We note that choosing the GPR  
745 antenna frequency that is best suited for identifying pedolith thickness is difficult,  
746 and calibration to local point locations (e.g., pedons) is always required.  
747 Furthermore, we found that the higher-frequency (1000 Mhz) antenna worked best  
748 for imaging pedolith layers for comparison to chemical indicators in the arid and  
749 semi-arid study areas (Pan de Azuár and Santa Gracia). In contrast, the lower  
750 frequency antenna (500 Mhz) worked better in the Mediterranean and temperate  
751 study areas (La Campana and Nahuelbuta) for imaging pedolith structure and for  
752 comparison to chemical observations.

753

754 ***Acknowledgement***

755 We would like to thank CONAF and all the Park Rangers for the possibility of working  
756 in the natural parks, for providing access to the sample locations, and help inside  
757 the National Parks. We also thank C. Pain, L. Worrall, and the topical editor D.  
758 Dunkerley for their reviews of an earlier version of the manuscript. We acknowledge  
759 support from the German Science Foundation (DFG) priority research program  
760 SPP-1803 “EarthShape: Earth Surface Shaping by Biota” (grants KR 3725/1-1,  
761 SCHA 1690/3-1, and EH329/17-2). RD was supported by a DFG Emmy Noether  
762 grant (DR 822/3-1).

763

764

765

766

767 **References:**

- 768 Aranha, P.R.A., Augustin, C.H.R.R., and Sobreira, F.G. The use of GPR for  
769 characterizing underground weathered profiles in the sub-humid tropics, *Journal*  
770 *of Applied Geophysics*, 49, 195-210, 2002.
- 771 Ardekani, M.R., Neyt, X., Benedetto, D., Slob, E., Wesemael, B., Bogaert, P.,  
772 Craeye, C., and Lambot, S. Soil moisture variability effect on GPR data,  
773 *Proceedings of the 15th International Conference on Ground Penetrating*  
774 *Radar*, Brussels, 214-217, doi: 10.1109/ICGPR.2014.6970416, 2014.
- 775 Armesto, J.J., Vidiella, P.E., and Gutierrez, J.R. Plant communities of the fog-free  
776 coastal desert of Chile: plant strategies in a fluctuating environment, *Revista*  
777 *Chilena de Historia Natural*, 66, 271-282, 1993.
- 778 Benedetto, A., and Pajewski, L. *Civil engineering applications of ground penetrating*  
779 *radar*, Springer, 2015.
- 780 Bernhard, N., Moskwa, L.-M., Oeser, R., von Blanckenburg, F., Boy, H., Brucker,  
781 E., Dippold, M., Ehlers, T.A., Fuentes-Espoz J.P., Godoy, R., Köster, M., Osses,  
782 P., Paulino, L., Schaller, M., Scholten, T., Seguel, O., Spielvogel, S., Spohn, M.,  
783 Stock, S., Stroncik, N., Uebernicketel, K., Wagner, D., Kühn, P.: Pedogenic and  
784 microbial interrelations to regional climate and local topography: New insights  
785 from a climate gradient (arid to humid) along the Coastal Cordillera of Chile,  
786 *Catena*, 170, 335-355, 2018.
- 787 Braun, J.-J., Descloitres, M., Riotte, J., Fleury, S., Barbiero, L., Boeglin, J.-L.,  
788 Violette, A., Lacarce, E., Ruiz, L., Sekhar, M., Mohan Kumar, M.S.,  
789 Subramanian, S., and Dupre, B. Regolith mass balance inferred from combined  
790 mineralogical, geochemical and geophysical studies: Mule Hole gneissic  
791 watershed, South India, *Geochimica et Cosmochimica Acta*, 73, 935-961, 2009.
- 792 Breiner, J.M., Doolittle J.A., Horton R., and Graham R.C. Performance of ground-  
793 penetrating radar on granitic regoliths with different mineral composition, *Soil*  
794 *Science*, 176, 435–440, 2011.
- 795 Brimhall, G.H., and Dietrich, W.E. Constitutive mass balance relations between  
796 chemical composition, volume, density, porosity, and strain in metasomatic  
797 hydrochemical systems: Results on weathering and pedogenesis, *Geochimica*  
798 *et Cosmochimica Acta*, 51 (3), 567-587, 1987.
- 799 Brimhall, G.H., Alpers, C., and Cunningham, A.B. Analysis of supergene ore-forming  
800 processes using mass balance principles, *Economic Geology*, 80, 1227-1254,  
801 1985.
- 802 Bristow, C.S., and Jol, H.M. An introduction to ground penetrating radar (GPR) in  
803 sediments, Geological Society, London, Special Publications 211, 1, 1-7, 2003.
- 804 Bristow, C.S., Jones, B.G., Nanson, G.C., Hollands, C., Coleman, M., and Price,  
805 D.M. GPR surveys of vegetated linear dune stratigraphy in central Australia:  
806 Evidence for linear dune extension with vertical and lateral accretion, *Special*  
807 *Papers- Geological Society of America*, 432, 19, 2007.
- 808 Carriere, S.D., Chalikakis, K., Senechal, G., Danquigny C., and Emblanch C.  
809 Combining electrical resistivity tomography and ground penetrating radar to

810 study geological structuring of karst unsaturated zone, *Journal of Applied*  
811 *Geophysics*, 94, 31-41, 2013.

812 Čeru, T., Dolonec, M., and Gosar, A. Application of Ground Penetrating Radar  
813 Supported by Mineralogical-Geochemical Methods for Mapping Unroofed Cave  
814 Sediments, *Remote Sensing* 10, 4, 639, 2018.

815 Chadwick, O.A., Brimhall, G.H., and Hendricks, D.M. From a black to a gray box - a  
816 mass balance interpretation of pedogenesis, *Geomorphology*, 3, 369-390,  
817 1990.

818 Dal Bo, I., Klotzsche, A., Schaller, M., Ehlers, A.T., Kaufmann, M.S., Fuentes-  
819 Espoz, J.P., Vereecken, H., van der Kruk, J. Geophysical imaging of regolith in  
820 landscapes along a climate and vegetation gradient in the Chilean Coastal  
821 Cordillera, *Catena*, 180, 146-159, 2019.

822 Daniels, D.J. Ground penetrating radar, *IEE Radar, Sonar, Navigation and Avionics*  
823 *Series*, The Institution of Electrical Engineers, 15, 2004.

824 De Benedetto, D., Castrignano, A., Sollitto, D., and Modugno, F. Spatial relationship  
825 between clay content and geophysical data, *Clay Minerals* 45, 2, 197-207, 2010.

826 De Coster, A., and Lambot, S. Fusion of Multifrequency GPR Data Freed From  
827 Antenna Effects, *Journal of Selected Topics in Applied Earth Observations and*  
828 *Remote Sensing*, 11 (2), 664-674, 2018.

829 Doolittle, J.A., and Collins, M.E. Use of soil information to determine application of  
830 ground penetrating radar. *Journal of Applied Geophysics*, 33 (1-3), 101-105,  
831 1995.

832 Doolittle, J.A., Minzenmayer, F.E., Waltman, F.W., Benham, E.C., Tuttle, J.W., and  
833 Peaslee, S.D. Ground-penetrating radar soil suitability map of the conterminous  
834 United States, *Geoderma*, 141, 416-421, 2007.

835 Estrada-Medina, H., Tuttle, W., Graham, R.C., Allen, M.F., and Jimenez-Osornio, J.  
836 Identification of Underground Karst Features using Ground-Penetrating Radar in  
837 Northern Yucatan, Mexico, *Vadose Zone Journal*, 9, 3, 653-661, 2010.

838 Ettinger, S., Manville, V., Kruse, S., and Paris, R. GPR-derived architecture of a  
839 labor-generated fan at Cotopaxi volcano, Ecuador, *Geomorphology*, 213, 225-  
840 239, 2014.

841 Fernandes Jr., A.L. Medeiros, W.E., Bezerra, F.H.R., Oliveira Jr., J.G., and Cazarin,  
842 C.L. GPR investigation of karst guided by comparison with outcrop and  
843 unmanned aerial vehicle imagery, *Journal of Applied Geophysics*, 112, 268-278,  
844 2015.

845 Gerber, R., Felix-Henningsen, P., Behrens, T., and Scholten, T. Applicability of  
846 ground-penetrating rader as a tool for nondestructive soil-depth mapping on  
847 Pleistocene slope deposits, *Journal of Plant Nutrition and Soil Science*, 173 (2),  
848 173-184, 2010.

849 Gomez, C., Kataoka, K.S., and Tanaka, K. Large-scale internal structure of the  
850 Sambongi Fan-Towada Volcano, Japan: Putting the theory to the test using PGR  
851 on volcanoclastic deposits, *Journal of volcanology and geothermal research*,  
852 229, 44-49, 2012.

853 Gómez-Ortiz, D., Martin-Crespo, T., Martin-Velazquez, S., Martinez-Pegan, P.,  
854 Higuera, H., and Manzana, M. Application of ground penetrating radar (GPR)  
855 to delineate clay layers in wetlands. A case study in the Soto Grande and Soto  
856 Chico watercourses, Donana (SW Soain), *Journal of Applied Geophysics*, 72, 2,  
857 107-113, 2010.

858 Green, A.G. Applications of 3-D georadar methods to diverse environmental and  
859 engineering problems, *Progress in Environmental and Engineering Geophysics*,  
860 edited by Chao, C. and Jianghai, X., Science Press USA, 220-226, 2004.

861 Guo, L., Chen, J., Cui, X., Fan, B., and Lin, H. Application of ground penetrating  
862 radar for coarse root detection and quantification: a review, *Plant Soil*, 362, 1-  
863 23, 2013.

864 Guo, L., Mount, G.J, Hudson, S., Lin, H., and Levia, D. Pairing geophysical  
865 techniques helps understanding of the near-surface Critical Zone: Visualization  
866 of preferential routing of stemflow along coarse roots. *Geoderma*, 357, 113953,  
867 2020.

868 Harari, Z. Ground-penetrating radar (GPR) for imaging stratigraphic features and  
869 groundwater in sand dunes, *Journal of Applied Geophysics*, 36, 1, 43-52, 1996.

870 Havholm, K.G., Bergstrom, N.D., Jol, H.M., and Running, G.L. GPR survey of a  
871 Holocene aeolian/fluvial/lacustrine succession, Lauder Sandhills, Manitoba,  
872 Canada, Geological Society, London, Special Publication 211, 47–54, 2003.

873 Heimsath, A.M., Dietrich, W.E., Nishiizumi, K., and Finkel, R.C. The soil  
874 production function and landscape equilibrium, *Nature*, 388, 358-361, 1997.

875 Heimsath, A.M., Dietrich, W.E., Nishiizumi, K., and Finkel, R.C. Cosmogenic  
876 nuclides, topography, and the spatial variation of soil depth, *Geomorphology*,  
877 27, 151-172, 1999.

878 Hilgard, E.W. *Soils: Their Formation, Properties, Compositions and Relations to*  
879 *Climate and Plant Growth in the Humid and Arid Regions*, The Macmillan  
880 Company, New York, 1914.

881 Holbrook, W.S., Riebe, C.S., Elwaseif, M., Hayes, J.L., Vasler-Reeder, K., Harry,  
882 D.L., Malazian, A., Dosseto, A., Hartsough, P.C., and Hopmans, W.  
883 Geophysical constraints on deep weathering and water storage potential in the  
884 Southern Sierra Critical Zone Observatory. *Earth Surface Processes and*  
885 *Landforms*, 39, 366-380, 2014.

886 Hruska, J., Cermak, J., and Sustek, S. Mapping tree root system with ground-  
887 penetrating radar. *Tree Physiology*, 19, 125-130, 1999.

888 Huisman, J.A., Hubbard, S.S., Annan, P.A. Measuring soil water content with  
889 ground penetrating radar: A review, *Vadose Zone Journal*, 2, 476-491,  
890 doi:10.2136/vzj2003.4760), 2003.

891 IUSS Working Group WRB. World reference base for soil resources 2014, update  
892 2015. Prepared by Schad P, van Huyssteen C, Micheli E. 192 pp. World Soil  
893 Resources Reports No. 106, FAO, Rome. 2015.

894 Jenny, H. *Factors of Soil Formation: A System of Quantitative Pedology*, Dover  
895 Publications, New York, 1994.

896 Jol, H.M. (Ed.): Ground penetrating radar: theory and applications, Elsevier Science,  
897 Amsterdam, the Netherlands ; Oxford, United Kingdom, 2009.

898 Kassambara, A. Practical guide to cluster analysis in R: unsupervised machine  
899 learning, STHDA, 2017.

900 Klotzsche, A, Jonard, F., Looms, M.C., van der Kruk, J., and Huisman, J.A.  
901 Measuring soil water content with ground penetrating radar: A decade of  
902 progress, *Vadose Zone Journal*, 17, 1, 1-9, 2018.

903 Lambot, S., Antoine, M., Vanclooster, M., Slob E.C. Effect of soil roughness on the  
904 inversion of off-ground monostatic GPR signal for noninvasive quantification of  
905 soil properties, *Water Resources Reseach*, 42, 3, 2006.

906 Langbein, W.B., and Schumm, S.A. Yield of sediment in relation to mean annual  
907 precipitation, *Transaction American Geophysical Union*, 39, 1076-1084, 1958.

908 Liu, J.L., and Marfurt, K.J. Instantaneous Spectral Attributes to Detect Channels,  
909 *Geophysics*, 72, 23-31.  
910 <http://dx.doi.org/10.1190/1.2428268>, 2007.

911 Mellett, J.S. Ground penetrating radar applications in engeneering, environmental  
912 management, and geology, *Journal of Applied Geophysics*, 33 (1-3), 157-166,  
913 1995.

914 Miller, T.W., Hendrickx, J.M.H., and Borchers, B. Radar detection of burried  
915 landmines field soils. *Vadose Zone Journal*, 3 (4). 1116-1127, 2002.

916 Mutz, S.G., Ehlers, T.A., Werner, M., Lehmann, G., Stepanek, C., and Li, J. Where  
917 is Late Cenozoic climate change most likely to impact denudation?, *Earth  
918 Surface Dynamics*, 6, 271-301, <https://doi.org/10.5194/esurf-2017-47>, 2018.

919 Nesbitt, H.W., and Young, G.M. Early Proterozoic climates and plate motions  
920 inferred from major element chemistry of lutites, *Nature*, 299, 215-217, 1982.

921 Oeser, R.A., Stroncik, N., Moskwa, L.-M., Bernhard, N., Schaller, M., Canessa, R.,  
922 van der B Rin, L., Köster, M., Brucker, E., Stock, S.S., Fuentes, J.P., Godoy, R.,  
923 Matus., F.J., Osés Pedraza, R., Osses McIntyre, P., Paulino, L., Seguel, O.,  
924 Bader, M.Y., Boy, J., Dippold, M.A., Ehlers, T.a., Kühn, P., Kuzyakiv, Y.,  
925 Peinweber, P., Scholten, T., Spielvogel, S., Spohn, M., Üubernickel, K.,  
926 Tielbörger, K., Wagner, D., and von Blanckenburg, F. Chemistry and  
927 microbiology of the Critical Zone along a steep climate and vegetation gradient  
928 in the Chilean Coastal Cordillera, *Ctena*, 170, 183-203, 2018.

929 Orlando, J., Comas, Z., Hynek, S., Buss, H.L., and Brantley, S.L. Architecture of the  
930 deep critical zone in the Rio Icacos watershed (Luquillo Critical Zone  
931 Observatory, Puerto Rico) inferred from drilling and ground penetrating radar  
932 (GPR), *Earth Surface Processes and Landforms*, 41, 13, 1823-1840, 2016.

933 Parsekian, A.D., Singha, K., Minsley, B.J., Holbrook, W.S., and Slater, L. Multiscale  
934 geophysical imaging of the critical zone, *Reviews of Geophysics*, 53, 1-26,  
935 2015.

936 Porder, S., Vitousek, M.P., Chadwick, O.A., Chamberlain, C. P. and Hilley, G.E.  
937 Uplift, Erosion, and Phosphorous Limitation in Terrestrial Ecosystems,  
938 *Ecosystems*, 10, 158-170, 2007.

939 Rabassa, J., and Clapperton, C.M. Quaternary glaciations of the southern Andes,  
940 Quaternary Science Reviews, 9, 153-174, 1990.

941 Roering, J.J., Kirchner, J.W., and Dietrich, W.E. Hillslope evolution by nonlinear,  
942 slope-dependent transport: Steady state morphology and equilibrium  
943 adjustment timescales, Journal of Geophysical Research, 106, B8, 16499-  
944 16513. 2001.

945 Roering, J.J., Marshall, J., Booth, A.M., Mort, M., and Jin, Q. Evidence for biotic  
946 controls on topography and soil production, Earth and Planetary Science  
947 Letters, 289, 183-190, 2010.

948 Saarenketo, T. Electrical properties of water in clay and silty soils. Journal of Applied  
949 Geophysics, 40, 73-88, 1998.

950 Sarkar, R., Paul, K.B., and Higgins, T.R. Impacts of soil physiochemical properties  
951 and temporal-seasonal soil-environmental status on ground-penetrating radar  
952 response. Soil Science Society of America Journal, 83, 542-554, 2019.

953 Scarpone, C., Schmidt, M.G., Bulmer, C.E., and Knudby, A. Modelling soil thickness  
954 in the critical zone for Southern British Columbia, Geoderma, 282, 59–69, 2016.

955 Schaller, M., Ehlers, T., Lang, K., Schmid, M., and Fuentes-Espoz, J. Addressing  
956 the contribution of climate and vegetation cover on hillslope denudation, Chilean  
957 Coastal Cordillera (26°–38° S), Earth and Planetary Science Letters, 489, 111-  
958 122, 2018.

959 Schmid, M., Ehlers, T.A., Werner, C., Hickler, T., and Fuentes-Espoz, J.-P. Effect  
960 of changing vegetation and precipitation on denudation – Part 2: Predicted  
961 landscape response to transient climate and vegetation cover over millennial to  
962 million-year timescales, Earth Surface Dynamics, 6(4), 859–881,  
963 doi:10.5194/esurf-6-859-2018, 2018.

964 Scott, K., and Pain, C. Regolith science, Csiro Publishing, 2009.

965 Sedgwick, P. Pearson's correlation coefficient, BMJ, 345:e4483, 2012.

966 Starke, J., Ehlers, T.A., and Schaller, M. Latitudinal effect of vegetation on erosion  
967 rates identified along western South America. Science, 367, 1358-1361, 2020.

968 Steelman, C.M., Endres, A.L., and Jones, J.P. High-resolution ground-penetrating  
969 radar monitoring of soil moisture dynamics: Field results, interpretation, and  
970 comparison with unsaturated flow model. Water Resour. Res. 48, W09538,  
971 doi:10.1029/2011WR011414, 2012.

972 Sucre, E.B., Tuttle, J.W., and Fox, T.R. The use of ground-penetrating radar to  
973 accurately estimate soil depth in rocky forest soils. Forest Science 57 (1), 59-  
974 66, 2011.

975 Telford, W.M., Geldart, L.P., Sheriff, R.E. and Keys, D.A. (Eds.): Applied  
976 Geophysics, 2th Edition, Cambridge University Press, Cambridge, 770.  
977 <http://dx.doi.org/10.1017/CBO9781139167932>, 1990.

978 Tosti, F., Patriarca, C., Slob, E., Benedetto, A., and Lambot, S. Clay content  
979 evaluation in soils through GPR signal processing. Journal of Applied  
980 Geophysics, 97, 69-80, 2013.

981 Utsi, E.C. Ground penetrating radar: theory and practice, Butterworth-Heinemann,  
982 2017.



983 van Dam, R.L., and Schlager, W. Identifying causes of ground-penetrating radar  
984 reflections using time-domain reflectometry and sedimentological analyses,  
985 *Sedimentology*, 47, 435–449, doi: 10.1046/j.1365-3091.2000.00304.x. 2000.

986 van Dam, R.L., Nichol, S.L., Augustinus, P.C., Parnell, K.E., Hosking, P.L., and  
987 McLean, R.F. GPR stratigraphy of a large active dune on Paren-garenga  
988 Sandspit, New Zealand, *The Leading Edge*, 22, 865–881, 2003.

989 Wang, P., Hu, Z., Zhao, Y., and Li, X. Experimental study of soil compaction effects  
990 on GPR signals, *Journal of Applied Geophysics*, 126m 128-137, 2016.

991 Wei, T. Package 'corrplot'-Visualization of a correlation matrix. v0.60. cran. rproject.  
992 org, 2012.

993 Werner, C., Schmid, M., Ehelrs, T.A., Fuentes-Espoz, J.P., Steinkamp, J., Forrest,  
994 M., Liakka, J., Maldonado, A., and Hickler, T. Effect of changing vegetation and  
995 precipitation on denudation - Part1; Predicted vegetation composition and cover  
996 over the last 21 thousand years along the Coastal Cordillera of Chile, *Earth  
997 Surface Dynamics*, 6, 829-858, <https://doi.org/10.5194/esurf-6-829-2018>, 2018.

998 Wold, S., Esbensen, K., and Geladi, P. Principal component analysis,  
999 *Chemometrics and intelligent laboratory systems*, 2, 37-52, 1987.

1000 Yoder, R.E., Freeland, R.S., Ammons, J.T., and Leonard, L.L. Mapping agricultural  
1001 fields with GPR and EMI to identify offsite movement of agrochemicals, *Journal  
1002 of Applied Geophysics*, 47, 3-4, 251-259, 2001.

1003 Zhang, J., Lin, H., and Doolittle, J. Soil layering and preferential flow impacts on  
1004 seasonal changes of GPR signals in two contrasting soils. *Geoderman*, 213,  
1005 560-569, 2014.

1006 Zhang, X., Dao, L., Zhang, C., Morrison, L., Hong, B., Zhang H., and Gan, Y.  
1007 Mapping the spatial distribution of soil depth in a grassland ecosystem with the  
1008 aid of ground penetrating radar and GIS (Northwestern Sichuan, China),  
1009 *Grassland Science*, 64, 4, 217-225, 2018.

1010  
1011  
1012

1013 **Figure captions**

1014 Fig. 1:

1015 Digital elevation model (Data source: GTOPO30) for the Chilean Coastal Cordillera  
1016 and the Central Andes showing the four investigated study areas (from north to  
1017 south): Pan de Azúcar (~26° S); Santa Gracia (~30° S); La Campana (~33° S); and  
1018 Nahuelbuta (~38° S).

1019

1020 Fig. 2:

1021 Satellite images (Data source: Google Earth©) of the four study areas from N to S  
1022 in latitude: A) Pan de Azúcar; B) Santa Gracia; C) La Campana; and D) Nahuelbuta.  
1023 Red stars indicate the pedon positions whereas the blue lines represent the  
1024 locations of the geophysical investigations.

1025

1026 Fig. 3:

1027 N- and S-facing hillslopes of the four study areas with locations of pedons and  
1028 transects of ground penetrating radar indicated by the red double arrows. For  
1029 complete characterization and interpretation of the pedons see Fig. 2 in Bernhard  
1030 et al. (2018) and Figs 3 to 6 in Oeser et al. (2018).

1031

1032 Fig. 4:

1033 Compilation of physical and chemical investigations with depth at the pedon location  
1034 in the mid-slope position of the S-facing hillslope in Pan de Azúcar. Properties  
1035 shown are: 1) GPR transect and the envelope profile of the 500 MHz measurement;  
1036 2) GPR transect and the envelope profile of the 1000 MHz measurement; 3) Bulk  
1037 density; 4) Grain size distribution of sand, silt, and clay; 5) Loss on ignition LOI; 6)  
1038 Chemical index of alteration CIA; 7) Chemical index of the mass transfer coefficient  
1039 Tau  $\tau$ ; and 8) volumetric strain  $\epsilon_{\text{strain}}$ . The black line indicates the boundary between  
1040 the mobile pedolith and the immobile saprolith (after Oeser et al., 2018) and the gray  
1041 area with green lines reflects the transition zone from B to C horizon (after Bernhard  
1042 et al., 2018).

1043

1044 Fig. 5:

1045 Primary component analysis PCA of properties for all four pedons in Pan de Azúcar.

1046 A) Scree plot showing the percentage of explained variances and B) Variables -

1047 PCA.

1048

1049 Fig. 6:

1050 Compilation of physical and chemical investigations at the pedon location in the mid-

1051 slope position of the S-facing hillslope in Santa Gracia. Properties shown are listed

1052 in caption of Fig. 4.

1053

1054 Fig. 7:

1055 Primary component analysis PCA of properties for all four pedons in Santa Gracia.

1056

1057 Fig. 8:

1058 Compilation of physical and chemical investigations at the pedon location in the mid-

1059 slope position of the S-facing hillslope in La Campana. Properties shown are listed

1060 in in caption of Fig. 4.

1061

1062 Fig. 9:

1063 Primary component analysis PCA of properties for all four pedons in La Campana.

1064

1065 Fig. 10

1066 Compilation of physical and chemical investigations at the pedon location in the mid-

1067 slope position of the S-facing hillslope in Nahuelbuta. Properties shown are listed

1068 as in caption of Fig. 4. Note that only the 500 MHz signal and envelope profile exist.

1069

1070 Fig. 11:

1071 Primary component analysis PCA of properties for all four pedons in Nahuelbuta.

1072

1073 Fig. 12:  
1074 A) 1000 MHz GPR transect and B) envelope for the S-facing hillslope in Pan de  
1075 Azúcar. The hillslope transect spans over ~20 m and includes pedon AZPED60,  
1076 AZPED50, and AZPED40 (black boxes). The potential pedolith thickness based on  
1077 the envelopes is indicated by stars (in B). The red bar indicates the B to C horizon  
1078 transition as given in Bernhard et al. (2018). Uphill is from left to right. Note that in  
1079 the radar data the air wave and background removal is applied.

1080  
1081 Fig. 13:  
1082 1000 MHz GPR signal and envelope for the mid-slope position of the S-facing  
1083 hillslope position in Santa Gracia (SGPED40). The hillslope transect spans over ~20  
1084 m. Interpretation of the radar signal are indicated where possible (stippled lines in A  
1085 and B). The potential pedolith thickness is indicated based on the envelope profile.  
1086 Uphill is from left to right. Lines and symbols in figures as described in Fig. 12.

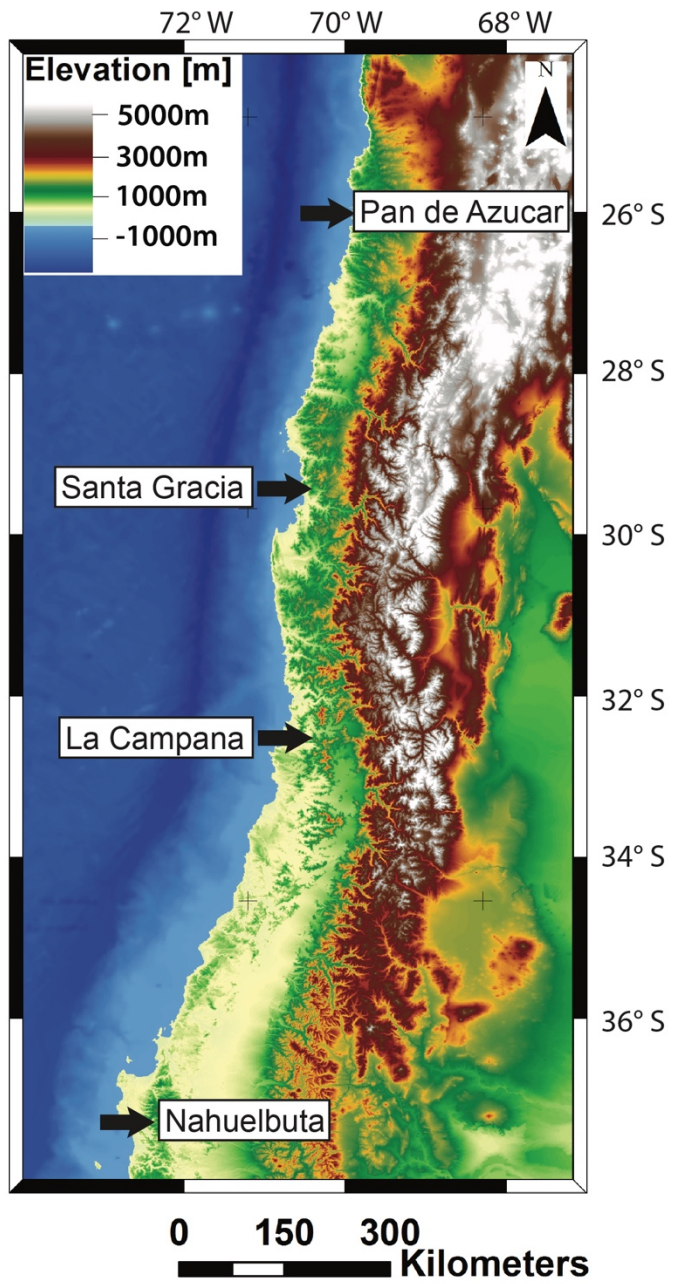
1087  
1088 Fig. 14:  
1089 500 MHz GPR signal and envelope for the mid-slope position of the S-facing  
1090 hillslope in La Campana (LCPED20). The hillslope transect spans over ~8 m.  
1091 Interpretation of the radar signal are indicated where possible (stippled and black  
1092 lines in A and B). The potential pedolith thickness is indicated based on the envelope  
1093 profile. Uphill is from left to right. Lines and symbols in figures as described in Fig.  
1094 12.

1095  
1096 Fig. 15:  
1097 500 MHz GPR signal and envelope for the mid-slope position of the S-facing  
1098 hillslope in Nahuelbuta (NAPED20). The hillslope transect spans over ~20 m.  
1099 Interpretation of the radar signal are indicated where possible (stippled lines in A  
1100 and B). The potential pedolith thickness is indicated based on the envelope profile.  
1101 Uphill is from left to right. Lines and symbols in figures as described in Fig. 12.

1102

1103

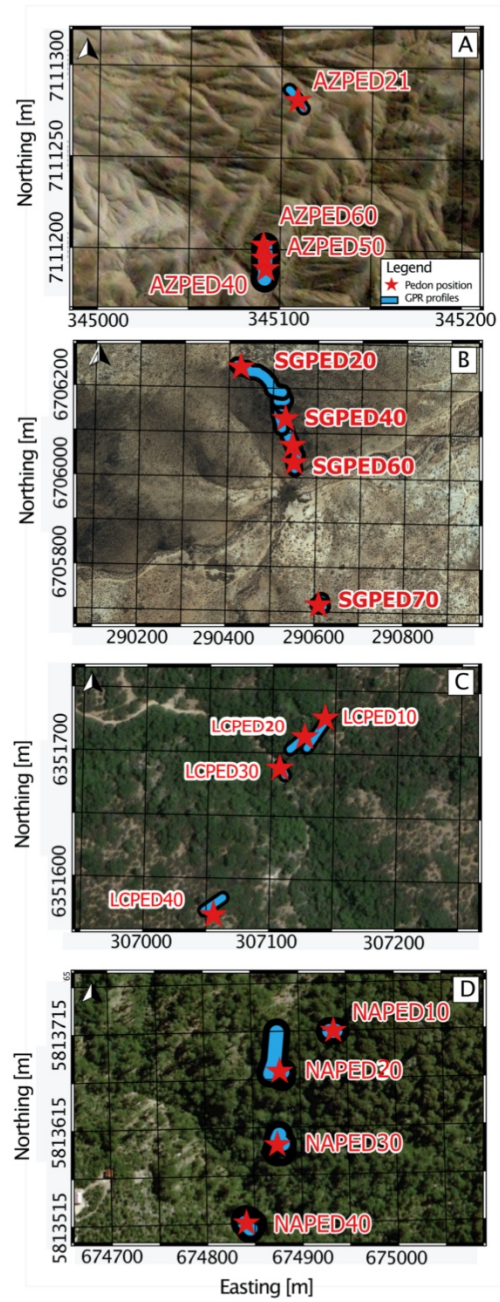
1104 Fig. 1:



1105

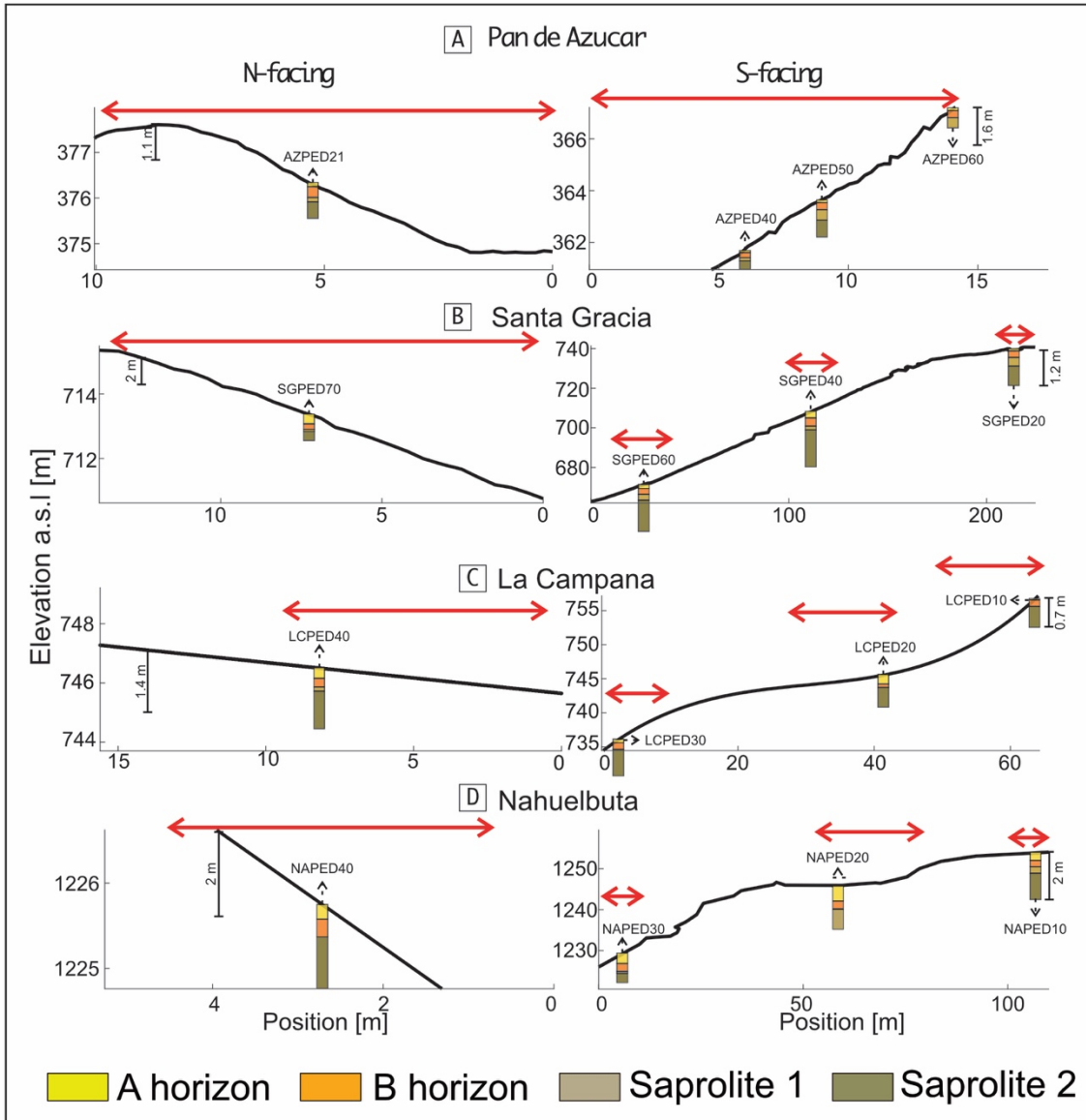
1106

1107 Fig. 2:



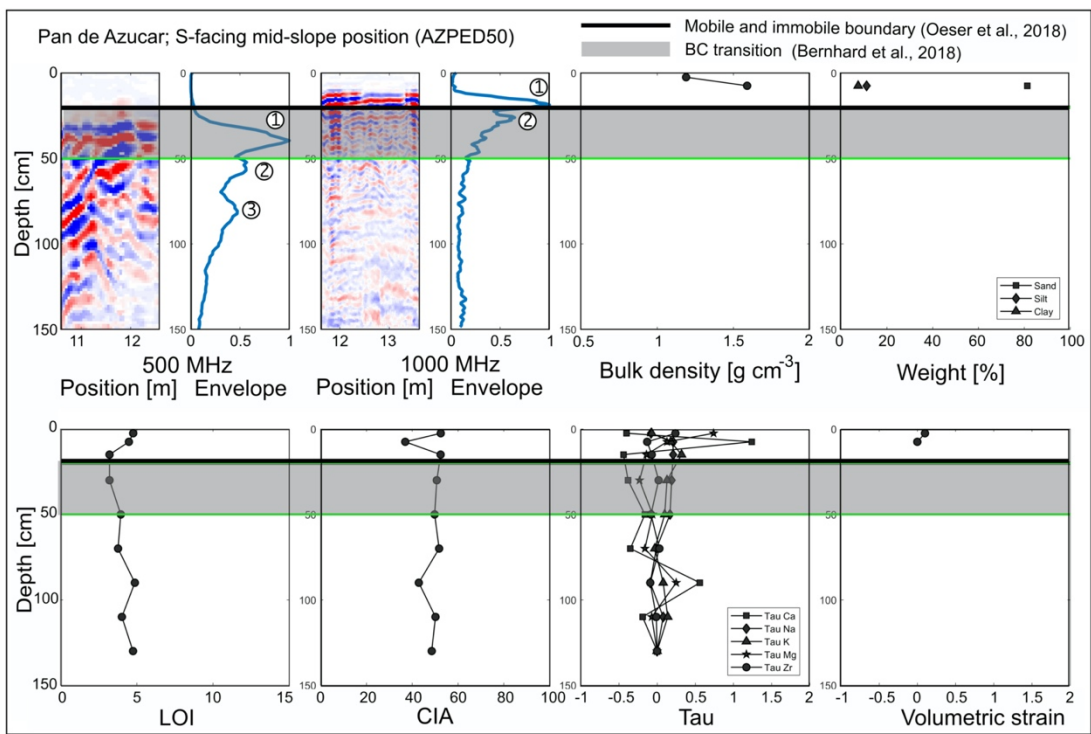
1108

1109 Fig. 3:



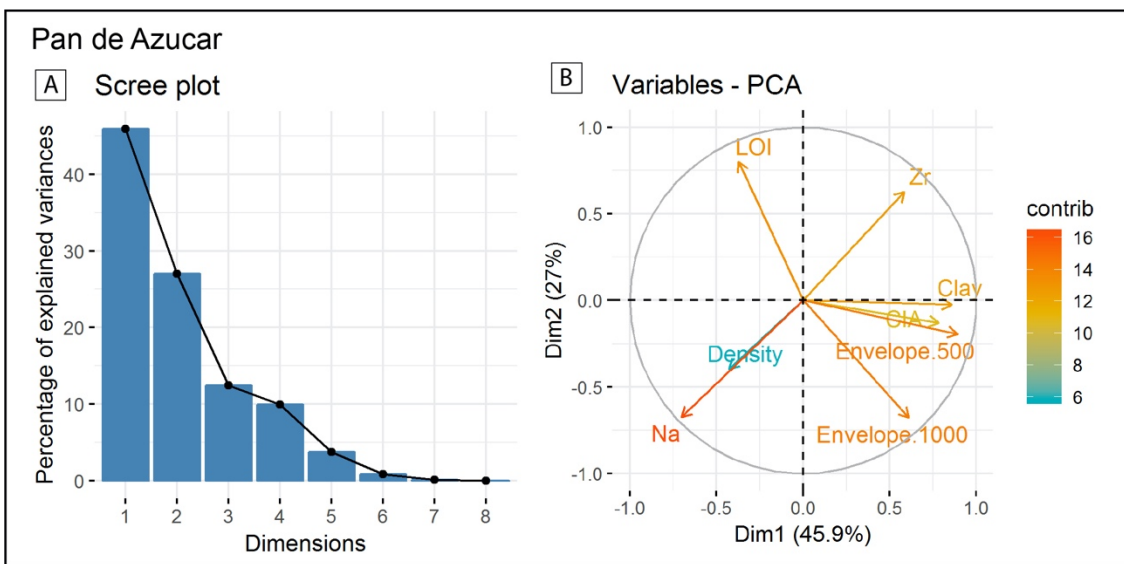
1110  
1111

1112 Fig. 4:



1113  
 1114  
 1115  
 1116

Fig. 5:

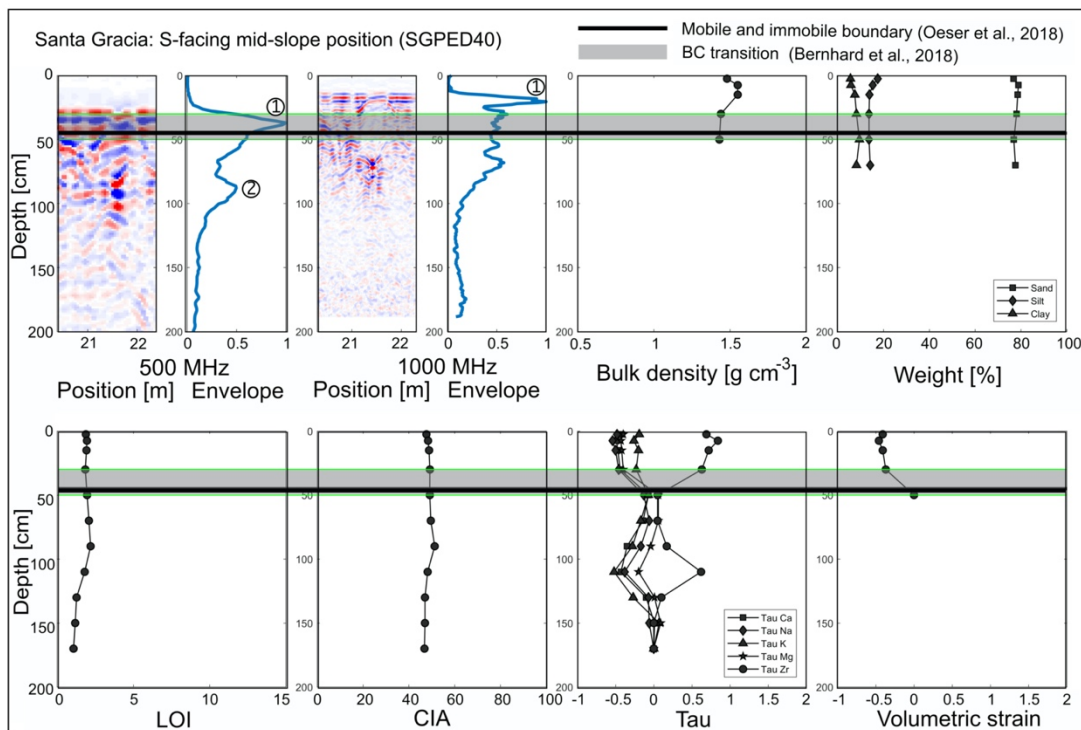


1117  
 1118  
 1119



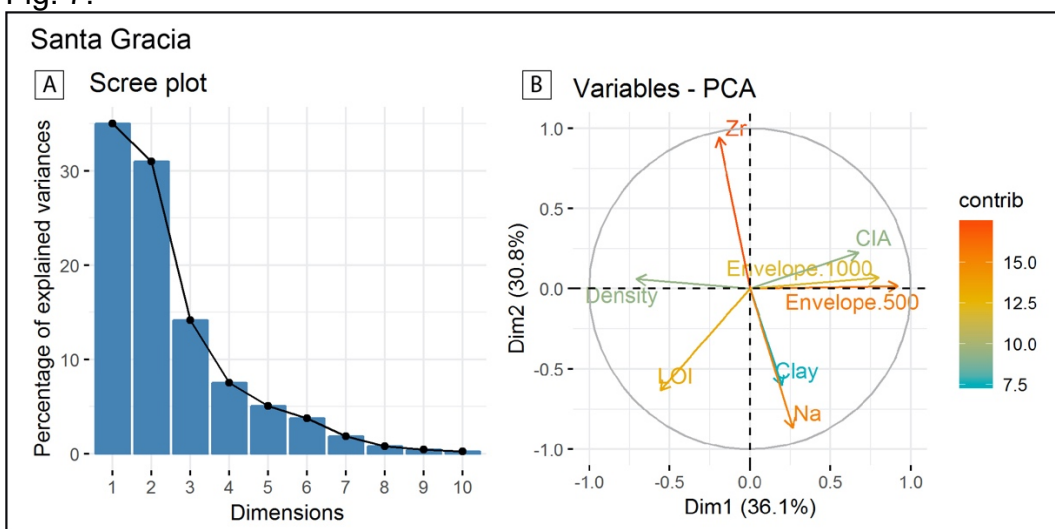
1120  
1121

Fig. 6:



1122  
1123  
1124

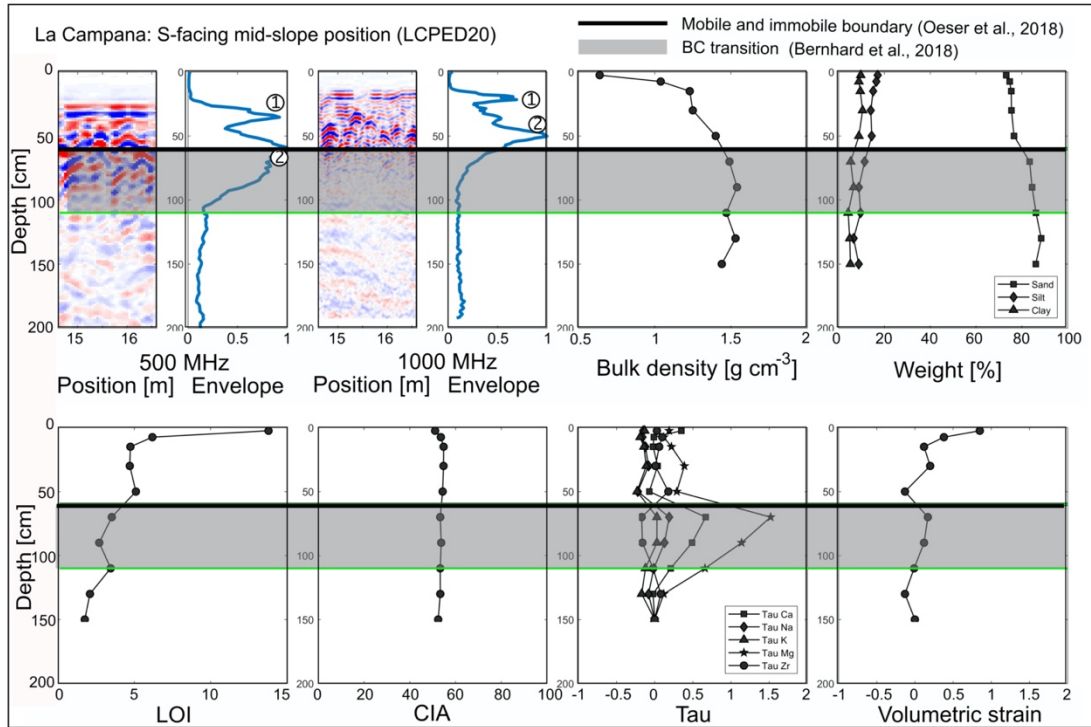
Fig. 7:



1125  
1126  
1127

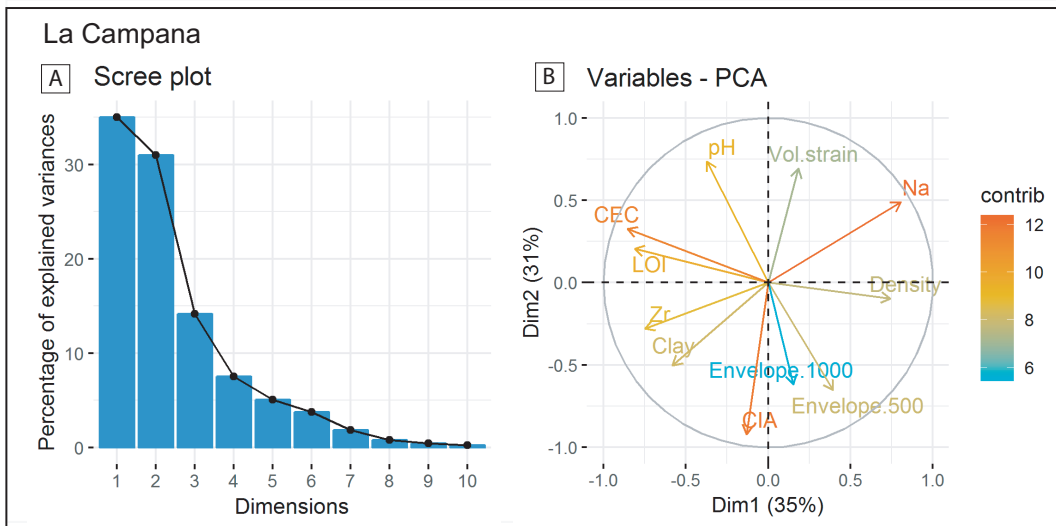
1128  
1129

Fig. 8:



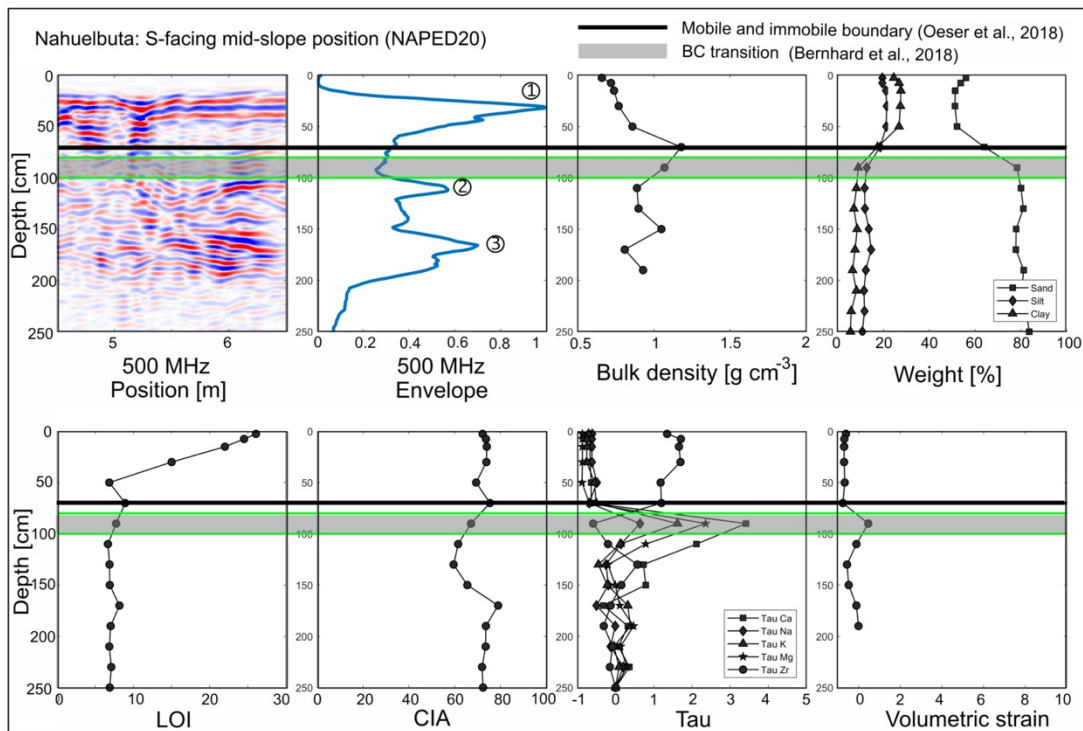
1130  
1131  
1132  
1133

Fig. 9:



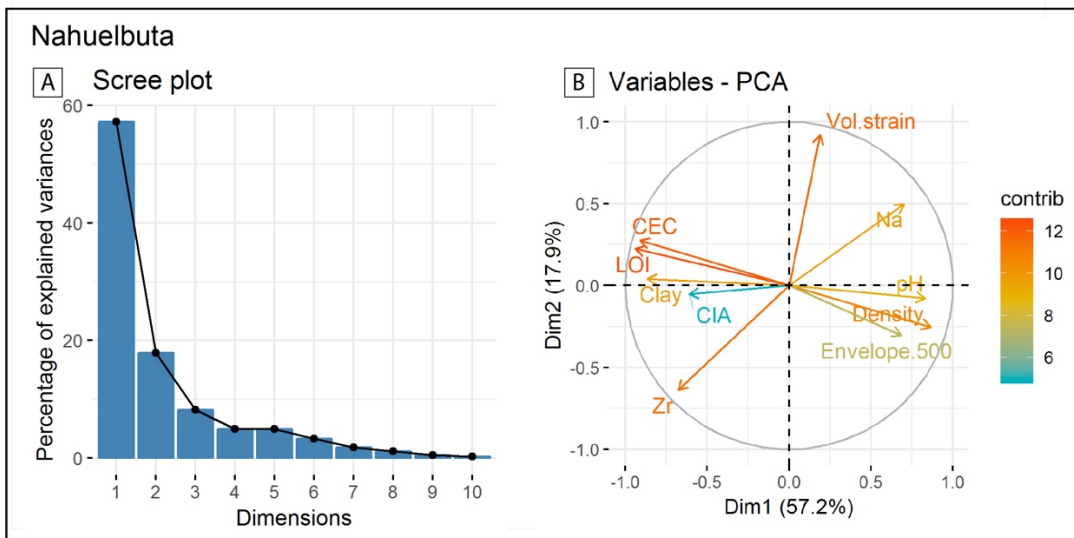
1134  
1135

1136 Fig. 10:



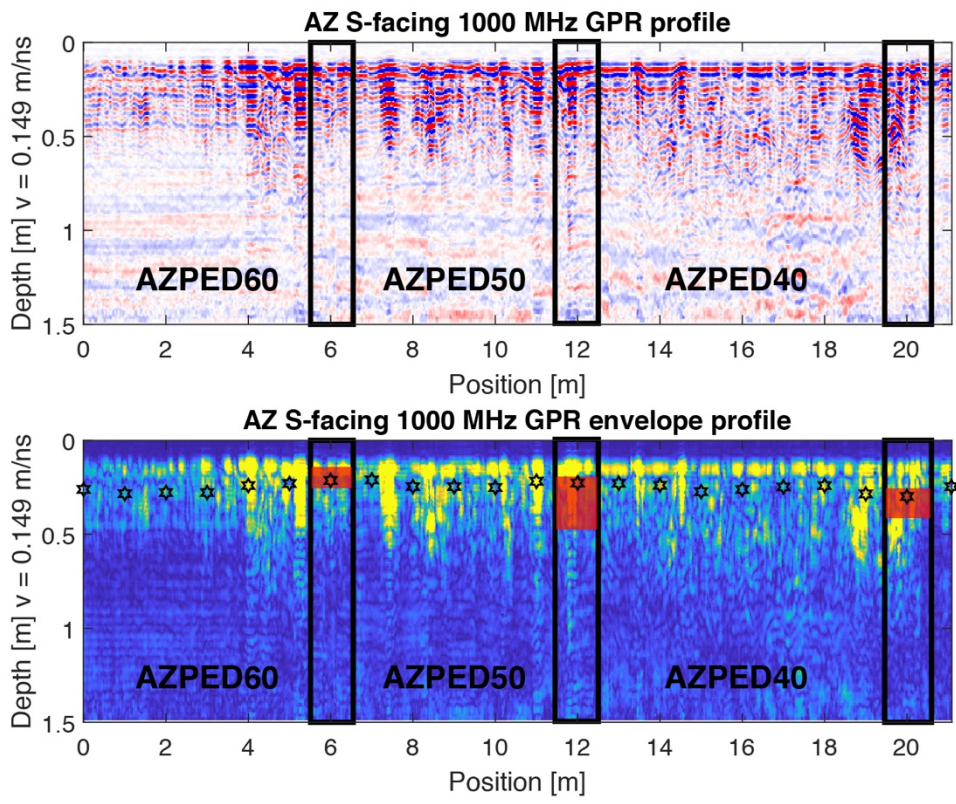
1137  
 1138  
 1139

Fig. 11:



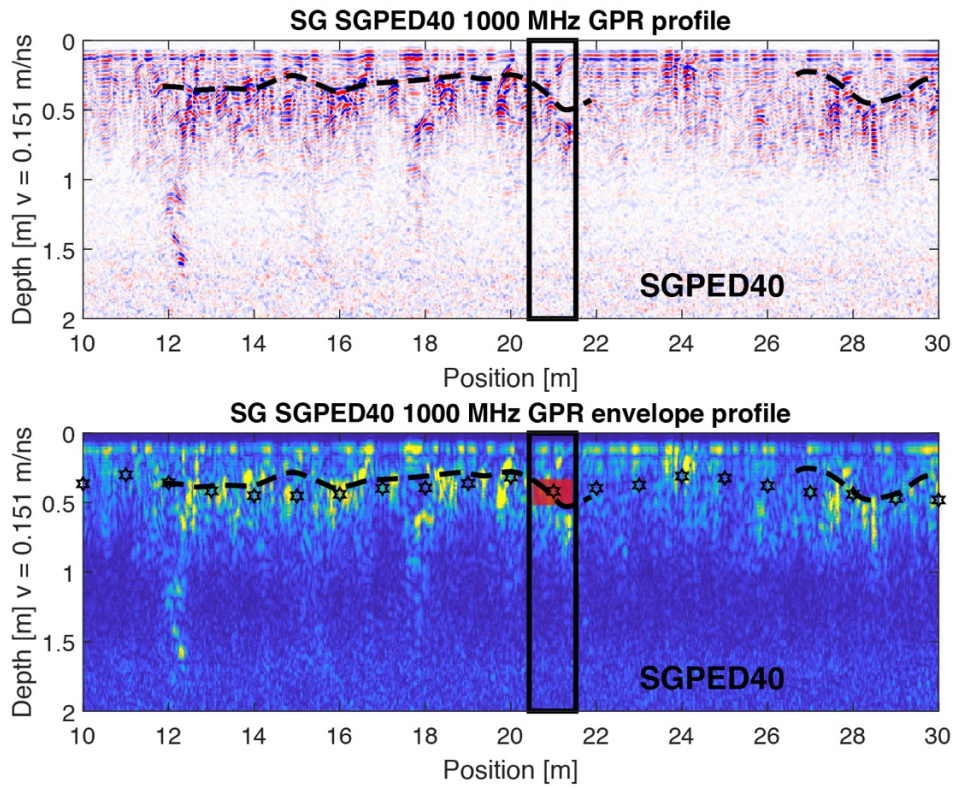
1140  
 1141  
 1142  
 1143

1144 Fig. 12:  
1145



1146  
1147  
1148

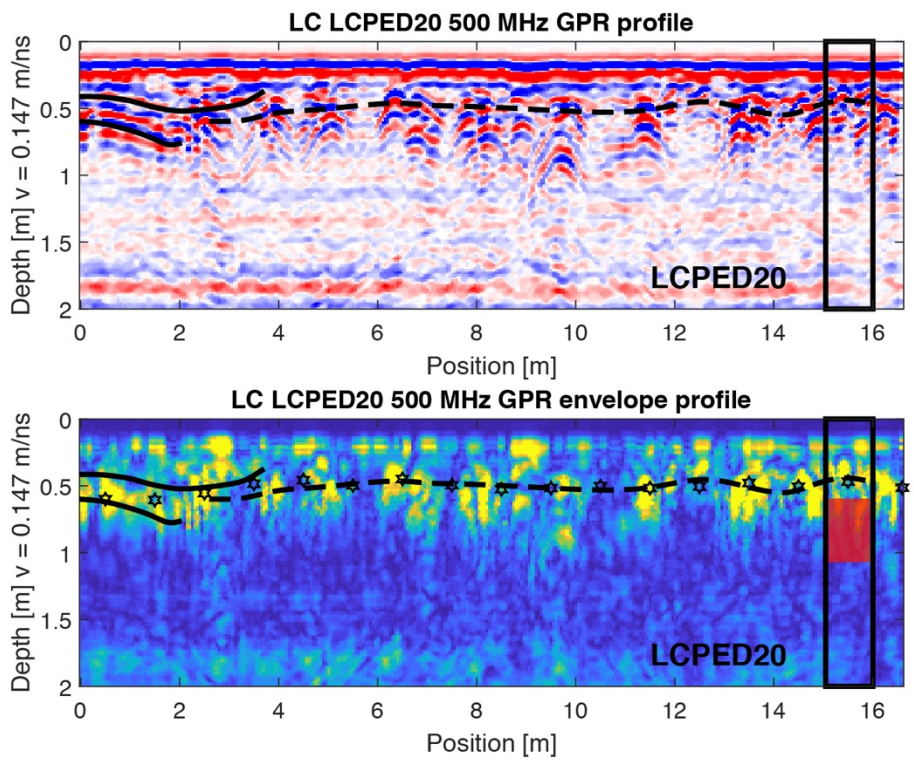
1149 Fig. 13:



1150  
1151

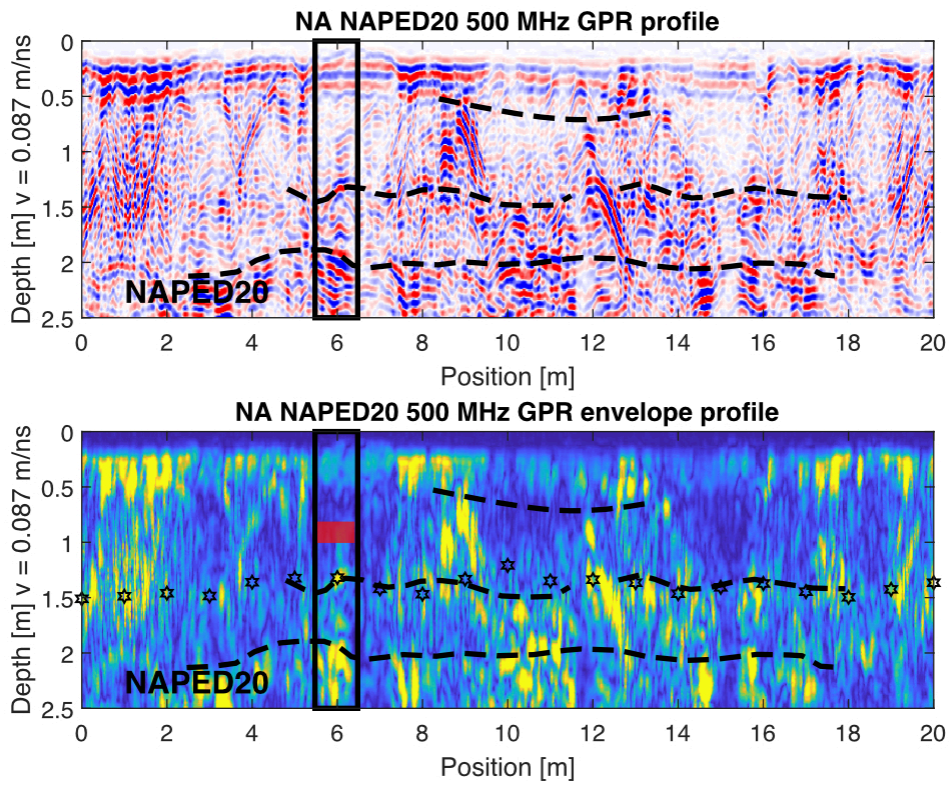


1152 Fig. 14:  
1153



1154  
1155  
1156

1157 Fig. 15:  
1158



1159  
1160

1161  
1162  
1163

Table 1:

Table 1: Data compilation for pedons in the investigated four study areas in the Chilean Coastal Cordillera														
Pedon	Location		Altitude m	Position	Aspect °	Slope °	Field observations			GPR point depth <sup>(5)</sup>		GPR transect depth <sup>(6)</sup>		
	°S	°W					BC-horizon transition <sup>(1)</sup> cm	Mobile/mmob. <sup>(2)</sup> cm	Mobile/mmob. <sup>(3)</sup> cm	GPR <sup>(4)</sup> cm	500 MHz cm	1000 MHz cm	500 MHz cm	1000 MHz cm
<b>Pan de Azucar</b>														
AZPED60	26.11012	70.54922	343	top	60	5	14-26		22	30-55 (?)	40	20/25/45		
AZPED50	26.11027	70.54922	333	mid	0	40	20-50	20		20-55	40/50/70	20/25/35/45	36 ± 1	25 ± 3
AZPED40	26.11024	70.54921	326	toe	0	33	23-40		25	20-40	40/55	20/30		
AZPED21	26.10936	70.54907	342	mid	180	25	20-30	20	20	30-45	37/55/75	20/30/45/55	40 ± 2	28 ± 7
<b>Santa Gracia</b>														
SGPED20	29.75636	71.16721	718	top	240	5	20-30		30	30	40	20/30/40/50	37 ± 5	34 ± 3
SGPED40	29.75738	71.16635	682	mid	0	25	30-50	50	45	60	45	20/30/40/55/65	40 ± 7	36 ± 5
SGPED60	29.75826	71.16615	638	toe	0	20	40-60		55	-	37/50	20/30	39 ± 7	35 ± 6
SGPED70	29.76120	71.16559	690	mid	180	15	25	35	35	NA	40	20/30	35 ± 3	28 ± 2
<b>La Campana</b>														
LCPED10	32.95581	71.06332	734	top	60	7	34		45	40/50	35/50/70	20/30/35/50/65	55 ± 6	44 ± 5
LCPED20	32.95588	71.06355	718	mid	0	23	60-110	60	60	50/60	35/60/70	20/38/50	59 ± 6	45 ± 4
LCPED30	32.95615	71.06380	708	toe	60	35	34-55		55	45/50	35/70	20/30/38	50 ± 9	41 ± 4
LCPED40	32.95720	71.06425	724	mid	120	12	36-103	35	35	-	35/65	20/30/40	56 ± 6	47 ± 6
<b>Nahuelbuta</b>														
NAPED10	37.80735	73.01285	1248	top	60	5	50-75		70	70/75	35/45/120		82 ± 15	
NAPED20	37.80770	73.01357	1239	mid	60	15	80-100	95	70	75/95	35/110/170		101 ± 8	
NAPED30	37.80838	73.01345	1228	toe	0	20	63-85		90	-	15/90/120/140		96 ± 6	
NAPED40	37.80904	73.01380	1200	mid	180	13	65-90	70	60	40/50	40/80/120		95 ± 11	
<sup>(1)</sup> Depth of BC-horizon transition from Bernhard et al., 2018														
<sup>(2)</sup> Depth of mobile pedolith from Schaller et al., 2018														
<sup>(3)</sup> Depth of mobile pedolith from Oeser et al., 2018														
<sup>(4)</sup> Depth based on data from Dal Bo et al., 2019														
<sup>(5)</sup> Depth based on single point GPR envelopes (This study)														
<sup>(6)</sup> Average depth based on envelopes from GPR transect data (This study)														

1164  
1165  
1166  
1167  
1168  
1169  
1170  
1171  
1172

Table 2:

Table 2: Overview of physical, chemical, and geophysical properties determined in the four different study areas				
Property	Abbreviation	Units	Meaning	Reference
Pedolith bulk density	$\rho_b$	g/cm <sup>3</sup>	Weight of unit volume	Bernhard et al., 2018
Grain size distribution	GSD	%	Weight percent of different grain sizes smaller than 2 mm	Bernhard et al., 2018
Potential hydrogen	pH		Acid and base properties	Bernhard et al., 2018
Cation exchange capacity	CEC	cmol <sub>c</sub> /kg	Soil ability to hold positively charged ions	Bernhard et al., 2018
Loss on ignition	LOI	%	Loss of volatiles due to excessiv heating	Oeser et al., 2018
Chemical index of alteration	CIA		Degree of weathering	Oeser et al., 2018
Mass transfer coefficient	$\tau$	m/s	Chemical gain or loss	Oeser et al., 2018
Volumetric strain	$\epsilon_{strain}$		Volumetric gain or loss	Oeser et al., 2018
Electric permittivity	$\epsilon_r$		Structural changes, porosity/soil water content	Dal Bo et al., 2019; This study
Electrical conductivity	$\sigma$	mS/m	Clay, salinity	Dal Bo et al., 2019; This study

1173  
1174  
1175  
1176  
1177  
1178



1179  
 1180  
 1181  
 1182  
 1183

Table 3:

Table 3: Correlation coefficients R of 1000 and 500 MHz GPR envelope with derivatives of physical and chemical properties for each study area										
Study area		Bulk density	Clay content	pH	CEC	LOI	CIA	Tau		Vol. strain
								Na	Zr	
1000 MHz										
Pan de Azucar	GPR	0.05	0.54			-0.1	-0.2	-0.1	-0.15	
Santa Gracia	GPR	-0.03	0.3			0.14	0.33	-0.16	0.1	
La Campana	GPR	-0.04	0.19	-0.34	-0.35	-0.19	0.43	-0.12	0.07	-0.18
Nahuelbuta	GPR									
Earth Shape	GPR	0.01	0.25	-0.15	-0.24	0.02	0	-0.14	0.01	
500 MHz										
Pan de Azucar	GPR	-0.29	0.17			-0.27	0.28	0.16	-0.07	
Santa Gracia	GPR	-0.39	0.26			-0.02	0.26	-0.08	0.02	
La Campana	GPR	0.2	0.22	-0.57	-0.39	-0.26	0.56	0.09	-0.26	-0.12
Nahuelbuta	GPR	0.74	-0.37	0.46	-0.53	-0.60	-0.24	0.21	-0.28	-0.01
Earth Shape	GPR	-0.16	-0.02	-0.39	-0.45	-0.03	0.45	0.11	-0.15	

1184